

BRL MR 2741

BRL

(Handwritten circled 'P' and '2')

AD

ADA 040433

MEMORANDUM REPORT NO. 2741

A NUMERICAL STUDY OF PROJECTILE
IMPACT ON EXPLOSIVES

M. S. Chawla
R. B. Frey

April 1977

DDC
JUN 10 1977
(Handwritten initials and 'A')

Approved for public release; distribution unlimited.

AD No. _____
DDC FILE COPY

USA ARMAMENT RESEARCH & DEVELOPMENT COMMAND
USA BALLISTIC RESEARCH LABORATORY
ABERDEEN PROVING GROUND, MARYLAND

Destroy this report when it is no longer needed.
Do not return it to the originator.

Secondary distribution of this report by originating
or sponsoring activity is prohibited.

Additional copies of this report may be obtained
from the National Technical Information Service,
U.S. Department of Commerce, Springfield, Virginia
22151.

The findings in this report are not to be construed as
an official Department of the Army position, unless
so designated by other authorized documents.

UNCLASSIFIED

SECURITY CLASSIFICATION OF THIS PAGE (When Data Entered)

9 REPORT DOCUMENTATION PAGE		READ INSTRUCTIONS BEFORE COMPLETING FORM
1. REPORT NUMBER BRL MEMORANDUM REPORT, NO. 2741	2. GOVT ACCESSION NO.	3. RECIPIENT'S CATALOG NUMBER
4. TITLE (and Subtitle) A NUMERICAL STUDY OF PROJECTILE IMPACT ON EXPLOSIVES		5. TYPE OF REPORT & PERIOD COVERED
7. AUTHOR(s) M. S./Chawla R. B./Frey		6. PERFORMING ORG. REPORT NUMBER
9. PERFORMING ORGANIZATION NAME AND ADDRESS USA Ballistic Research Laboratory Aberdeen Proving Ground, MD 21005		8. CONTRACT OR GRANT NUMBER(s)
11. CONTROLLING OFFICE NAME AND ADDRESS US Army Materiel Development & Readiness Command 5001 Eisenhower Avenue Alexandria, VA 22333		10. PROGRAM ELEMENT, PROJECT, TASK AREA & WORK UNIT NUMBERS 16. IW161102AH43
14. MONITORING AGENCY NAME & ADDRESS (if different from Controlling Office) 14. BRL-MR-2741		12. REPORT DATE 13. APRIL 1977
		13. NUMBER OF PAGES 70
		15. SECURITY CLASS. (of this report) UNCLASSIFIED
		15a. DECLASSIFICATION/DOWNGRADING SCHEDULE
16. DISTRIBUTION STATEMENT (of this Report) Approved for public for release; distribution unlimited.		
17. DISTRIBUTION STATEMENT (of the abstract entered in Block 20, if different from Report)		
18. SUPPLEMENTARY NOTES		
19. KEY WORDS (Continue on reverse side if necessary and identify by block number)		
20. ABSTRACT (Continue on reverse side if necessary and identify by block number) HELP code is employed to study the impact of a projectile on heavily confined, inert, solid explosive Comp B3. Temperature rise due to shock compression and plastic deformation, in both the explosive and the metal confinement, is estimated. In addition, the effect of variation of the impact parameters, such as projectile diameter, projectile velocity and confinement thickness on the rise in temperature is studied. It is concluded that usually shock is a dominant mechanism responsible for significant heating of the		

DD FORM 1 JAN 73 1473

EDITION OF 1 NOV 65 IS OBSOLETE

UNCLASSIFIED

SECURITY CLASSIFICATION OF THIS PAGE (When Data Entered)

050 750

213

UNCLASSIFIED

SECURITY CLASSIFICATION OF THIS PAGE(When Data Entered)

20. (Continued)

explosive. However, in certain situations, plastic deformations may lead to violent reaction in confined explosives.

A

UNCLASSIFIED

SECURITY CLASSIFICATION OF THIS PAGE(When Data Entered)

TABLE OF CONTENTS

	Page
LIST OF ILLUSTRATIONS	5
LIST OF TABLES	7
I. INTRODUCTION	9
II. BRIEF DESCRIPTION OF THE NUMERICAL TECHNIQUE FOR EVALUATING TEMPERATURE RISE IN EXPLOSIVE	12
A. The HELP Code	12
B. Material Model	12
1. Equation of State	12
2. Elastic-Plastic Constitutive Relationship and Yield Criterion	16
3. Failure Criterion	16
C. Calculation of Plastic Work	16
D. Calculation of Shock Temperature	20
III. RESULTS	21
A. Typical Case	21
B. Parametric Study	33
1. Effect of Projectile Size	38
2. Effect of Projectile Velocity	38
3. Effect of Casing Thickness	38
C. Effect of Reduction of Cell Size	44
D. Effect of High Tensile Strength	44
E. Effect of Presence of Cracks or Notches in Explosive Material	47
IV. CONCLUSION	47
V. RECOMMENDATIONS FOR FUTURE WORK	48

TABLE OF CONTENTS (Continued)

	Page
REFERENCES	49
APPENDICES	
A. Equation of State of Comp B3	51
B. Material Constants for Comp B3	59
C. Walsh-Christian Technique	61
LIST OF SYMBOLS	65
DISTRIBUTION LIST	67

LIST OF ILLUSTRATIONS

Figure	Page
1. Drop-weight Test of a Layer of Granular PETN Viewed in Transmitted Light	10
2. Area Weighting for Calculation of Plastic Work Associated With a Massless Lagrangian Tracer	19
3. The Projectile/Explosive/Casing Configuration at the Beginning of the Impact for the Typical Problem	23
4. The Projectile/Explosive Casing Configuration at 60 μ s After The Impact for the Typical Case	24
5. Compression Map at 60 μ s for the Typical Case	25
6. Pressure Map at 60 μ s for the Typical Case	26
7. Radial Velocity Map at 60 μ s for the Typical Case	27
8. Axial Velocity Map at 60 μ s for the Typical Case	28
9. Specific Internal Energy Map at 60 μ s for the Typical Case	29
10. Map of the Highest Temperature of Cell at 60 μ s for the Typical Case	30
11. Map of the Highest Explosive Temperature of Cell at 60 μ s For the Typical Case	31
12. Plot of Temperature Rise of Steel and Explosive for the Typical Case	32
13. Pressure versus Time Plot at the Explosive Interface for the Typical Case	34
14. Pressure versus Time at the Projectile/Casing Interface for The Typical Case	35
15. Dissipation of Shock Inside the Target for the Typical Case	36
16. Metal and Explosive Plastic-work Temperatures versus Time For $r = 0.25, 0.50$ and 1.00 cm	39
17. Total Plastic Work in Explosive versus Projectile Radius At $t = 40$ μ s	40
18. Explosive Shock Temperature versus Projectile Radius	41

LIST OF ILLUSTRATIONS (Continued)

Figure	Page
19. Metal and Explosive Plastic-work Temperatures versus Time For $v = 1.0, 2.0, 3.0$ km/s	42
20. Explosive Shock Temperature versus Projectile Velocity	43
21. Metal and Explosive Temperatures versus Casing Thickness	45
22. Metal and Explosive Plastic-work Temperatures versus Cell Size	46
A-1. A Plane, One-dimensional Shock Wave	54
A-2. Equation-of-State Surfaces	57
A-3. Curve Fitting of the Hugonist Pressure of Comp B3	58

LIST OF TABLES

Table	Page
I. Elastic Modulus, Yield Strength and Failure Criterion . . .	13
II. Equation of State Constants for Steel	15
III. The Test Matrix for the Parametric Study	37
A-I. Shock Wave Data for Comp B3	52

I. INTRODUCTION

The objective of this paper is to evaluate the relative importance of shock heating and plastic work in the initiation of explosives by projectile impact. There is some confusion about this issue due to the large variety of impact tests which are conducted on explosives. To eliminate some of this confusion and to delineate the situation which we are considering, we will first describe some of the tests which have been used and what is known about the initiation mechanism in each.

A number of different phenomena fall under the broad topic, "impact initiation of explosives". The term impact initiation is frequently used to describe drop weight tests. These tests are distinguished by having a thin sample of explosive sandwiched between a large drop weight (projectile) and a rigid anvil. The velocities and pressures required for initiation in such experiments are very low (generally less than 5 meters/sec and 10 kb respectively). In this type of test, Heavens and Fields¹ and Afanasev and Bobolev² have demonstrated that initiation occurs as the result of adiabatic deformation of the thin samples (Figure 1). Their work indicates that plastic and/or viscous flow play an essential role in the initiation process. Mechanical shock is unimportant under these conditions.

In a second type of experiment a flying plate impacts an explosive charge which is sandwiched, at the time of impact, between the flying plate and a rigid anvil. In this type of experiment the diameter of the flying plate is large compared to the thickness of the charge, but the charge dimensions are much greater than in the drop weight tests. Such experiments have been performed by Napadensky³ and analyzed numerically by Kot, et al⁴. In the experiments, two results were observed. Above a certain velocity detonation occurs within a few microseconds as a result of the incident or reflected shock. Below this velocity explosions,

1. S. N. Heavens and J. E. Fields, *Proceedings of the Royal Society*, A338, 77, 1974.
2. G. T. Afanasev and V. K. Bobolev, "Initiation of Solid Explosives by Impact," U.S. Department of Commerce, Springfield, VA, 1971.
3. H. S. Napadensky, "Initiation of Explosives by Low Velocity Impact," *Fourth Symposium on Detonation*, U.S. Naval Ordnance Laboratory, White Oak, MD, 1965.
4. C. A. Kot, H. A. Napadensky, Y. A. Shikari, and A. H. Wiedermann, "A Numerical Study of Impact Phenomena in Explosives and Propellants," *Proceedings of the International Conference on Computational Methods in Nonlinear Mechanics*, University of Texas, Austin, TX, 1974.

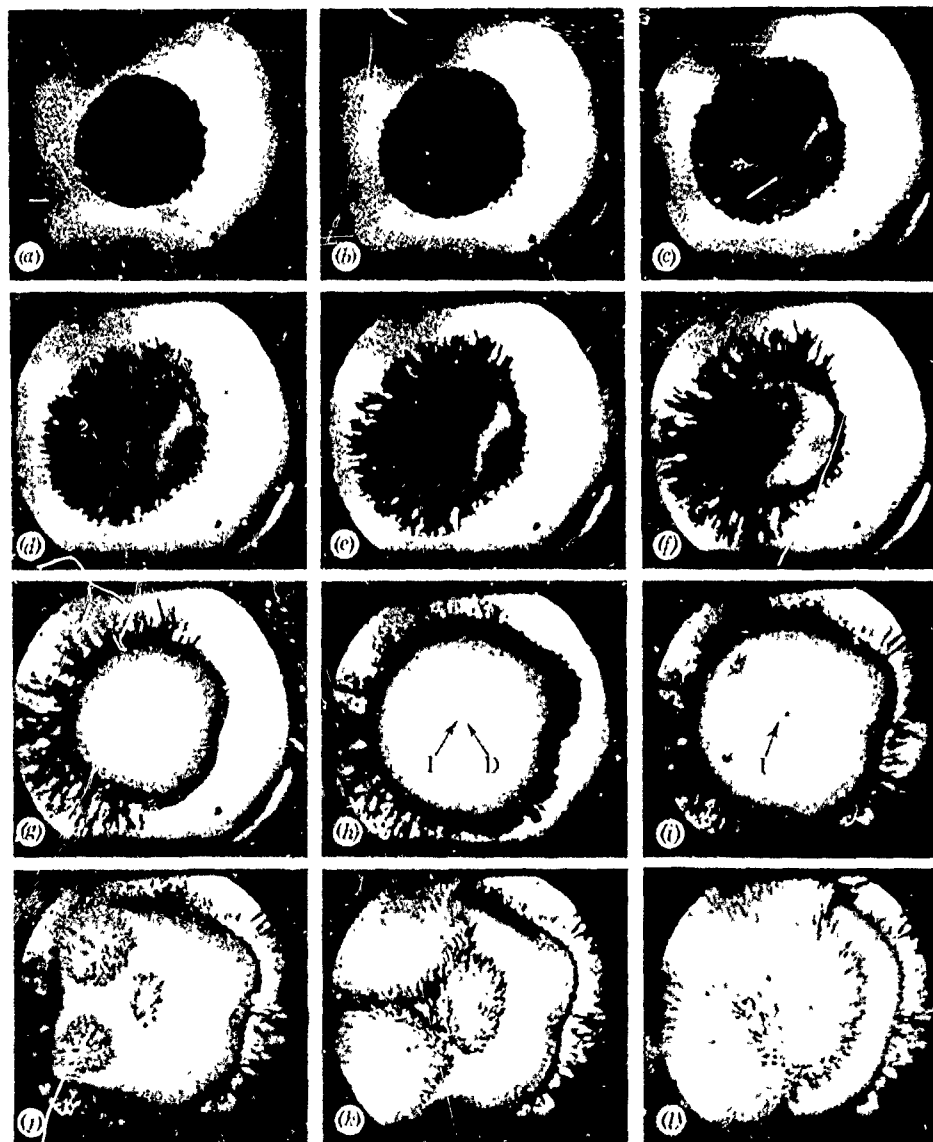


Figure 1. Drop Weight Test of a Layer of Granular PETN Viewed in Transmitted Light. Interframe Time is $5.5 \mu\text{s}$. (Photograph Taken From Ref. 1)

but not detonations may occur after the explosive has been extruded laterally. The shock initiation process has been studied by many investigators and is qualitatively understood. Ignition occurs at hot spots which are formed in the explosive behind the shock and the resultant energy release accelerates the shock towards detonation. From a microscopic point of view, plastic and viscous flows in the neighborhood of voids are necessary preconditions for shock initiation, but from a macroscopic point of view deformation is not important. The initiation of low order explosions is not so well understood, but it seems probable that macroscopic deformation is involved in a crucial way. Kot, in his numerical analysis of the experiments, observed that material strength had an insignificant effect on the temperatures generated by the shock in the explosive. He concluded that energy dissipation due to distortion was of little importance. However, his calculations did not extend to times large enough for significant macroscopic distortion to occur, and his conclusion does not apply to initiation of low order explosions.

A third experimental geometry involves impacts by projectiles which are small in all dimensions compared to the dimensions of the receptor charge. Bullet impact tests are typically of this type. Such tests may be performed with either confined or unconfined explosives. Brown and Whitbread⁵ and Dewey and Slade⁶ performed and analyzed this type of test for charges which were unconfined or confined only on the impacted surface. With such charges one observes either that the charge detonates or is shattered and the result is recorded as no reaction. Dewey and Slade, and Brown and Whitbread, demonstrated that in this situation the initiation occurs as a result of the shock generated at impact and macroscopic material deformations are not important. However, when fully confined charges are impacted, explosions which are not detonations can occur, and these reactions can occur with impact velocities which are much below those required for detonation⁷. The times required for the occurrence of these low order reactions are long (several hundred microseconds), and it is possible that material heating due to macroscopic deformation of the charge may play some role in the initiation process.

In this paper we focus our attention on the latter type of experiment where the charge is fully confined and the charge dimensions are large compared to those of the projectile. We are particularly interested in the mechanism leading to low order explosions as opposed to detonations. At the onset of this work, we expected that plastic

-
5. S. Brown and E. Whitbread, *Les Ondes de Detonation*, 1961.
 6. J. Dewey and D. Slade, *BRL Report 1021*, 1957.
 7. R. Frey, G. Melani, M. Chawla, and J. Trimble, "Initiation of Violent Reactions by Projectile Impact," *Sixth Symposium on Detonation*, San Diego, CA, 1976.

work might be an important mechanism in those situations where the thickness of the confinement on the impacted surface is large compared to the radius of the projectile. In this situation the shock becomes weak before reaching the explosive. We were interested not only in a comparison of shock and deformational heating, but also in the trends of deformational heating with projectile radius and velocity. In this paper we have considered only elastic-perfectly plastic materials. Viscous effects will be considered later.

II. BRIEF DESCRIPTION OF NUMERICAL TECHNIQUE FOR EVALUATING THE TEMPERATURE RISE IN EXPLOSIVE

A. The HELP Code

The principal analytic tool employed in this numerical study was the HELP⁸ code, which is a finite difference, multimaterial Eulerian computer program dealing with compressible fluids and elastic-perfectly plastic flows in two space dimensions and time. Although the code is basically Eulerian, free surfaces and material interfaces are treated in a Lagrangian fashion throughout the computational grid. No material diffusion is permitted across these discrete interfaces. In the past, the HELP code has been used to solve a variety of problems, in the area of fragmenting munitions, hypervelocity impact, and shaped charge jet formation.

B. Material Model

The material model employed in HELP consists of an equation of state, a deviatoric constitutive relationship, a yield criterion and a failure criterion for each of the material packages employed in the problem. The materials of interest here are steel for the projectile and the casing and unreacted solid Comp B3. Table I provides values of some of the parameters employed in the calculation. The main features of HELP are discussed briefly in the following subsections. The CGS system of units is employed in HELP code. Therefore, no attempt is made here to convert the input/output of HELP to any other system of units.

1. Equation of State. For the unreacted explosive, Comp B3, a Mie-Grüneisen equation of state was employed. This equation is fully described in Appendix A and assumes the Grüneisen parameter, γ to be a constant. The form of the equation is

$$P = (A\mu + B\mu^2 + C\mu^3) + \gamma\rho E \quad (1)$$

8. L. J. Hageman, D. E. Wilkins, R. T. Sedgwick and J. L. Waddell, "HELP: A Multi-Material Eulerian Program for Compressible Fluid and Elastic-Plastic Flows in Two Space Dimensions and Time," Systems, Science & Software Report No. SSS-R-75-2654, 1975.

Table I. Elastic Modulus, Yield Strength and Failure Criterion

MATERIAL PROPERTY	STEEL	SOLID COMP B3
ρ_0 (g/cm ³)	7.80	1.68
G (dyne/cm ²)	1.93×10^{12}	5.03×10^{10}
Y_0 (dyne/cm ²)	6.00×10^9	5.10×10^8
Y_1 (dyne/cm ²)	0	0
Y_2 (dyne/cm ²)	0	0
E_m (erg/g)	3.00×10^{10}	1.13×10^9
$(\rho/\rho_0)_{MIN}$	0.97	0.99

where P is pressure, E is specific internal energy, $\mu \equiv \rho/\rho_0 - 1$. In order to ensure that the pressure is tensile for expanded states, ($\mu < 0$), equation (1) was modified to read

$$P = (A\mu - B\mu^2 + C\mu^3) + \Gamma\rho E \quad (2)$$

In equations (1) and (2)

$$\begin{aligned} A &= 13.5 \times 10^{10} \text{ (dyne/cm}^2\text{)} \\ B &= 9.5 \times 10^{10} \text{ (dyne/cm}^2\text{)} \\ C &= 100.6 \times 10^{10} \text{ (dyne/cm}^2\text{)} \\ \Gamma &= 0.947 \end{aligned} \quad (3)$$

For steel, a Tillotson equation of state was employed in order to describe the condensed, the expanded and the transitional states. For the condensed states, i.e. for $\mu > 0$ or for any cold states, $E < E_s$, the equation has the form

$$P = P_c = \left[a + \frac{b}{\frac{E}{E_0\eta^2} + 1} \right] E\rho + A\mu + B\mu^2 \quad (4)$$

For expanded hot states, i.e. for $\mu < 0$ and $E > E'_s$, the equation of state has the form

$$P = P_E = aE\rho + \left[\frac{bE\rho}{\frac{E}{E_0\eta^2} + 1} + A\mu e^{-\beta\left(\frac{\rho}{\rho_0} - 1\right)} \right] e^{-\alpha\left(\frac{\rho}{\rho_0} - 1\right)^2} \quad (5)$$

In Equations (4) and (5) $\eta \equiv \rho/\rho_0 = \mu + 1$. A smooth transition between the condensed and the expanded states is obtained from an interpolated form valid for $E_s < E < E'_s$ and $\mu < 0$. This transition region equation of state has the following form

$$P = P_T = \frac{(E - E_s) P_E + (E'_s - E) P_c}{E'_s - E_s} \quad (6)$$

In equations (1) through (6), A, B, C, α , β , a, b, E_s , E'_s and ρ_0 are constants for the particular material. The values of these constants for steel are listed in Table II.

Table II. Equation of State Constants for Steel⁸

$$a = .5$$

$$b = 1.5$$

$$A = 1.28 \times 10^{12} \text{ dyne/cm}^2$$

$$B = 1.05 \times 10^{12} \text{ dyne/cm}^2$$

$$E_0 = 0.095 \times 10^{12} \text{ erg/g}$$

$$\alpha = 5$$

$$\beta = 5$$

$$\rho_0 = 7.8 \text{ g/cm}^3$$

$$E_S = 2.44 \times 10^{10} \text{ erg/g}$$

$$E'_S = 10.2 \times 10^{10} \text{ erg/g}$$

2. Elastic-Plastic Constitutive Relation and Yield Criterion. The deviatoric stress increments, ds_{ij} are determined by using the elasticity relationship

$$ds_{ij} = 2Gde_{ij} \quad (7)$$

where G is the rigidity modulus and de_{ij} are increments of deviatoric strain. When any increment of stress causes the Von-Mises yield condition

$$s_{ij}s_{ij} \leq 2Y^2 \quad (8)$$

to be violated, each stress component is proportionately reduced to bring the stress state normally back to the yield surface. A variable yield strength incorporating work hardening and thermal softening is defined to be

$$Y = (Y_0 + Y_1\mu + Y_2\mu^2) \left(1 - \frac{E}{E_m}\right) \quad (9)$$

In equation (9), Y_1 and Y_2 are the coefficients of work hardening terms and E_m is the melt energy.

3. Failure Criterion. A material is said to have failed in HELP, if the material compression falls below a critical value indicated by $(\rho/\rho_0)_{MIN}$. The critical material compression is defined by⁹

$$\left(\frac{\rho}{\rho_0}\right)_{MIN} = -\frac{S}{\kappa} + 1 \quad (10)$$

where S is the material spall threshold and κ is its bulk modulus. All the stresses in a cell are zeroed out if its compression ratio, ρ/ρ_0 is less than $(\rho/\rho_0)_{MIN}$. The values of failure criteria for the two materials employed in the code are listed in Table I.

C. Calculation of Plastic Work

In order to discuss the calculation of plastic work in any material package, it will be necessary to review the important computational steps employed in the HELP code. A complete theoretical description of the HELP code is given in Reference 8. For each computational cell of

9. R. T. Sedgwick, J. L. Waddell, M. Baker and J. M. Walsh, "Studies of Erosion and Impact Resistance of ABM Materials," BRL Contract Report No. 301, 1976.

the Eulerian grid in HELP, the conservation equations determine mass, momentum and total energy at any time cycle. These equations are

$$\frac{\partial}{\partial t} \int_V \rho \, dV = - \int_S \rho \, u_i \, n_i \, dS \quad (11)$$

$$\frac{\partial}{\partial t} \int_V \rho \, u_j \, dV = \int_S \sigma_{ij} \, n_i \, dS - \int_S \rho \, u_i \, u_j \, n_i \, dS \quad (12)$$

$$\frac{\partial}{\partial t} \int_V \rho \, E_T \, dV = \int_S \sigma_{ij} \, u_j \, n_i \, dS - \int_S \rho \, u_i \, E_T \, n_i \, dS \quad (13)$$

where

$$E_T = \frac{1}{2} u_i \, u_i + E \quad (14)$$

is the specific total energy, E is the specific internal energy, σ_{ij} are the stresses, u_i are the velocities and ρ is the density. The volume and surface integrals in above equations refer to integration over the volume and surface area of the cells in the grid. It is convenient to express the total stresses as made up of two parts; hydrostatic and deviatoric, i.e.

$$\sigma_{ij} = s_{ij} - \delta_{ij} \, P \quad (15)$$

Employing the finite-differencing scheme along with equation (15), one obtains from equations (11) through (13)

$$\Delta m = - \Delta t \int_S \rho \, u_i \, n_i \, dS \quad (16)$$

$$\begin{aligned} \Delta(m \, u_j) &= \Delta t \int_S s_{ij} \, n_i \, dS - \Delta t \int_S P \, n_j \, dS \\ &\quad - \Delta t \int_S (\rho \, u_i \, u_j) \, n_i \, dS \end{aligned} \quad (17)$$

$$\begin{aligned} \Delta(m \, E_T) &= \Delta t \int_S s_{ij} \, n_i \, u_j \, dS - \Delta t \int_S P \, u_i \, n_i \, dS \\ &\quad - \Delta t \int_S (\rho \, u_i \, E_T) \, n_i \, dS \end{aligned} \quad (18)$$

The three terms on the right respectively represent increments on the cell surfaces due to the stress deviatoric forces, the hydrostatic pressure forces and the contribution due to transport. These increments in mass, momenta and energy are calculated in three distinct phases of the computation. These phases are

- S PHASE where the effects of material strength are considered
- H PHASE where the effects of pressure are taken into account
- T PHASE where the effects of material transports are studied

In the absence of material strength, no plastic work will be done on the material. The plastic work is the contribution to the internal energy from the S phase. As seen from equations (16) and (17), the total energy is calculated from equation

$$\Delta_S (m E_T) = \Delta t \int s_{ij} u_j n_i dS \quad (19)$$

while the momentum is calculated from

$$\Delta_S (m u_j) = \Delta t \int s_{ij} n_i dS \quad (20)$$

Starting from equations (19) and (20), the contribution to plastic work for each cycle is easily obtained. The plastic work increment of any cell i in the S phase during a time cycle n is given by

$$\Delta W_i^n = \Delta E_{T_i}^n - \Delta \left(\frac{1}{2} u_j^n u_j^n \right) \quad (21)$$

Because of the material flow, the plastic work and, consequently, the temperature rise could be grossly in error if care is not taken to follow the material motion. In this study, a feature of the plugging version of HELP was employed. In the plugging version four Lagrangian, massless tracer particles are placed in each cell of a subgrid of the problem. The subgrid is chosen to contain the portion of the material package that undergoes most deformation. In time, the tracers move with the velocity of the material and migrate to different cells. An area-weighted average is used to update the plastic work of the material associated with each tracer. Consider, for example a point 0 in Figure 2. The plastic work, W_0 , associated with point 0 at time-cycle n is defined as

$$W_0^n = W_0^{n-1} + \frac{\sum_{i=1}^4 A_i \Delta W_i^n}{\sum_{i=1}^4 A_i} \quad (22)$$

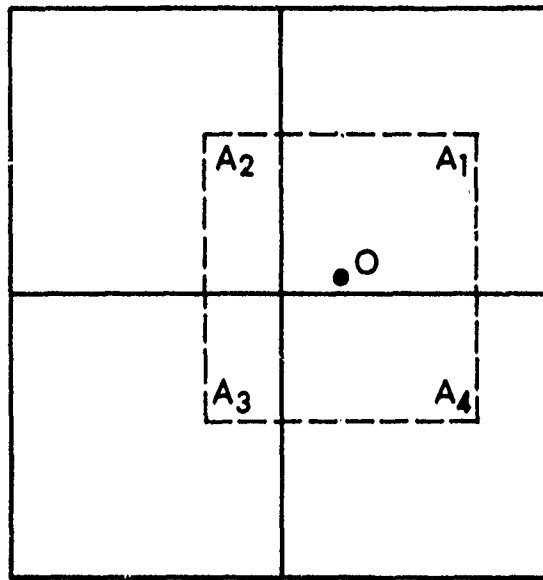


Figure 2. Area Weighting for Calculation of Plastic Work Associated With a Massless Lagrangian Tracer.

where A_i is the overlap area of the fictitious cell centered at the point 0 with cell i , ΔW_i^n is the specific plastic work increment associated with center of cell i during cycle n .

In the plugging version, once the plastic work associated with one or more points in the region of space spanned by the tracer exceeds a predetermined cutoff value, PLWMIN, the plug is allowed to propagate. Propagation of the plug was inhibited in this study by arbitrarily setting the plastic work cutoff value too high.

Since the plastic deformation of the material is irreversible, it is safe to assume that all of the plastic work is converted into heat. The temperature rise due to plastic work is then easily calculated, for a cell centered around the point 0, from the equation

$$T_0^n = \frac{W_0^n}{J C_v} \quad (23)$$

In equation (23), J is the mechanical equivalent of heat and C_v is the specific heat. It should be noted that each cycle makes a positive contribution to equation (23). The plastic temperature will cease to rise whenever the material fails in tension or melts. In both cases shear stresses as well as the hydrostatic pressures are zeroed out. The temperature will also cease to rise if the material stops deforming.

D. Calculation of Shock Temperature

When a strong compression wave is transmitted into metal, the internal energy and therefore the temperature of the material increases. It is assumed that material strength plays a negligible role at this stage since the shock pressures are usually several hundred times the yield strength of the material. Moreover, it is assumed that in a time of 10^{-7} seconds or less, thermodynamic equilibrium is established for the material behind the shock front, so that the state of material behind the shock front can be described by an equilibrium temperature.

The Walsh-Christian technique¹⁰ used here to calculate the shock temperature of steel and explosive is described in detail in Appendix C of this report. The shock temperature is easily calculated from the expression

$$T(V_H) = T_0 e^{b(V_0 - V_H)} + e^{-bV_H} \int_{V_0}^{V_H} \left[\frac{e^{bV} f(V)}{C_v} \right]_{HUG} dV \quad (24)$$

10. J. M. Walsh and R. H. Christian, *Phys Rev*, 97, 1544, 1955.

where

$$b = \Gamma/V_0 \quad (25)$$

and

$$f(V) = \frac{1}{2} \frac{dP}{dV} (V_0 - V) + \frac{1}{2} P \quad (26)$$

The pressure and the derivative of pressure in equation (26) are readily evaluated from the equation of state of the material under consideration and the resulting integral in equation (24) is computed numerically. After attaining the peak temperature, the material expands adiabatically, without exchange of energy with the outside world. Temperature during this process of expansion therefore drops and is given by

$$T = T_H e^{-b(V_H - V)} \quad (27)$$

where (T_H, V_H) are the temperature and volume of the shock heated material, while (T, V) are the temperature and volume of the adiabatically cooled material. In order to calculate the residual shock temperatures of the materials, equations (24) and (27) are to be employed with appropriate code values for the volumes, V_0 , V_H and V .

III. RESULTS

This section describes the results of a series of numerical experiments that were performed using the HELP code. The quantities of interest are the interfacial pressure, shock pressure and plastic work temperature. Since the explosive in this study was always confined in a steel box, it was therefore possible to calculate all of the above quantities for the explosive as well as the steel.

However, it must be stressed that the numerical values obtained using HELP code may not be completely dependable until a thorough analysis of computational errors introduced by finite zone-size, mismatched-impedance, artificial viscosity, etc. is made. Also, the code cannot predict the temperature of hot spots which might be formed by intergranular friction or other mechanisms. The purpose of this study has been to arrive at some useful conclusions regarding the trends as a result of variation of impact parameters such as the projectile diameter, the projectile velocity and the casing thickness. The material description employed here is approximate, at best. The results, therefore, may or may not match the experiments. Each calculation reported here required a core of 120 K decimal and computing time in excess of 12 hours on a Univac 1108.

A. Typical Case

The typical set-up of the problem consisted of a cylinder of unreacted Comp B3 explosive, which was 5 cm in radius and 5 cm high.

The explosive was completely enclosed in a 1/2 cm thick steel casing. The explosive/steel assembly was impacted by a projectile which was 2 cm in length and 1 cm in diameter. The impact velocity was 1 km/sec. The impact took place along the axis of symmetry of the problem, thus it was sufficient to study only half of the total geometry. The computational grid consisted of 28 x 48 cells. In the z-direction the cell size was 0.2 cm while in the r-direction the cell size changed progressively from 0.1 cm to 0.5 cm. The cell size in the regime of greatest deformation was 0.1 x 0.2 cm. Figure 3 depicts the initial projectile/explosive/casing configuration employed in this calculation. This figure also shows the four tracers per cell which are used to monitor the plastic work of a cell. The tracer particles were placed only in a portion of the entire grid. Figure 4 shows the deformation of the projectile and target at 60 μ s after the impact. Figure 5 shows the compression of the entire grid at $t = 60 \mu$ s. At this time almost all of the cells in the grid have acquired normal or less than normal densities indicating extensive material failure. Figure 6, which is a plot of pressure in the projectile and target, indicates that most of the high pressure regions in the grid are tensile. Figures 7 and 8 show the radial and axial velocities at $t = 60 \mu$ s. At this time the projectile has lost most of its velocity and the crater lip formed in the target is moving in a direction opposite to that of the projectile. Figure 9 is a pictorial map of the specific internal energy. Figures 10 and 11 are the maps of plastic temperatures of the grid. The temperature maximas of all the tracers that have migrated into a given cell are plotted in Figure 10. For pure cells, Figure 10 shows either the maximum temperature of the steel or the explosive. The temperatures, in general, are lower in explosive than in steel, mainly because the specific heat of the explosive is roughly three times that of the steel and because the explosive yield strength is an order of magnitude lower than the steel yield strength. In the mixed cells, containing both steel and explosive, the maximum temperature will correspond to a steel tracer. Figure 11 shows only the temperature maxima of the explosive; the steel temperatures are completely blanked out. The highest temperatures are found always to belong to the tracers which were initially placed at the casing interface. In 60 μ s, most of these tracers have moved away from their initial locations.

Figure 12 is a plot of the highest temperature rise versus time for both the steel casing and the undetonated explosive. For each material, a high peak in temperature rise corresponding to its shock pressure is obtained in a short time after the impact. The shock temperature acquired its highest value in the steel a little earlier than in the explosive but drops quite drastically shortly thereafter in both materials. At about 10 μ s each of the materials begins to deform plastically and starts to heat up. The temperature at the hottest point in the flow is plotted in Figure 12. The highest temperature at late times may be in a portion of material which was cooler at early times. In other words, the temperatures sketched in Figure 12 may belong to different portions of material at different times. The rise in plastic temperatures levels off at 62°C for the explosive and at 190°C for the steel. The following observations can be made with respect to Figure 12.

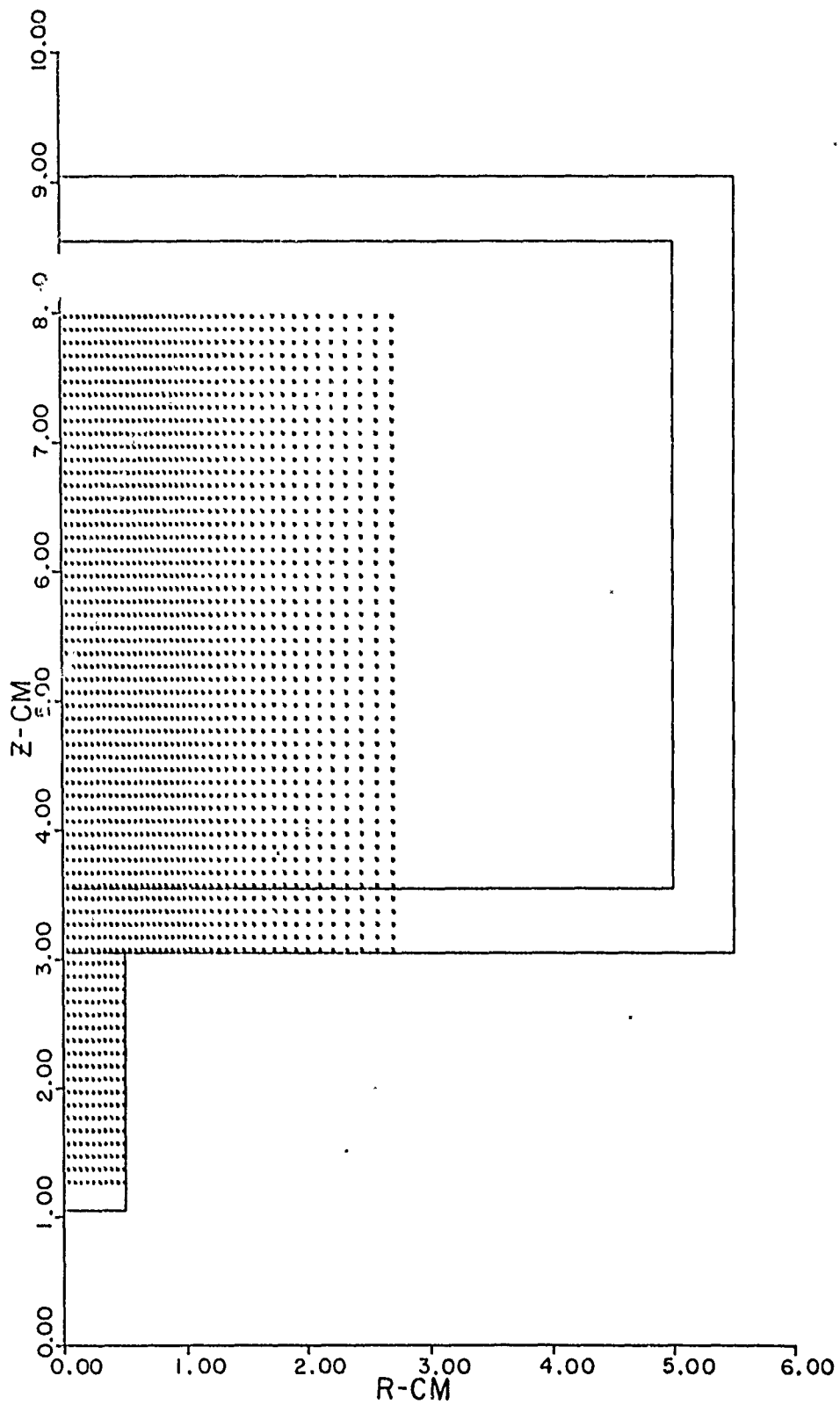


Figure 3. The Projectile / Explosive / Casing Configuration at the Beginning of the Impact for the Typical Problem.
 (Impact Velocity = 1 km/s, Rad of Projectile = 0.5 cm)

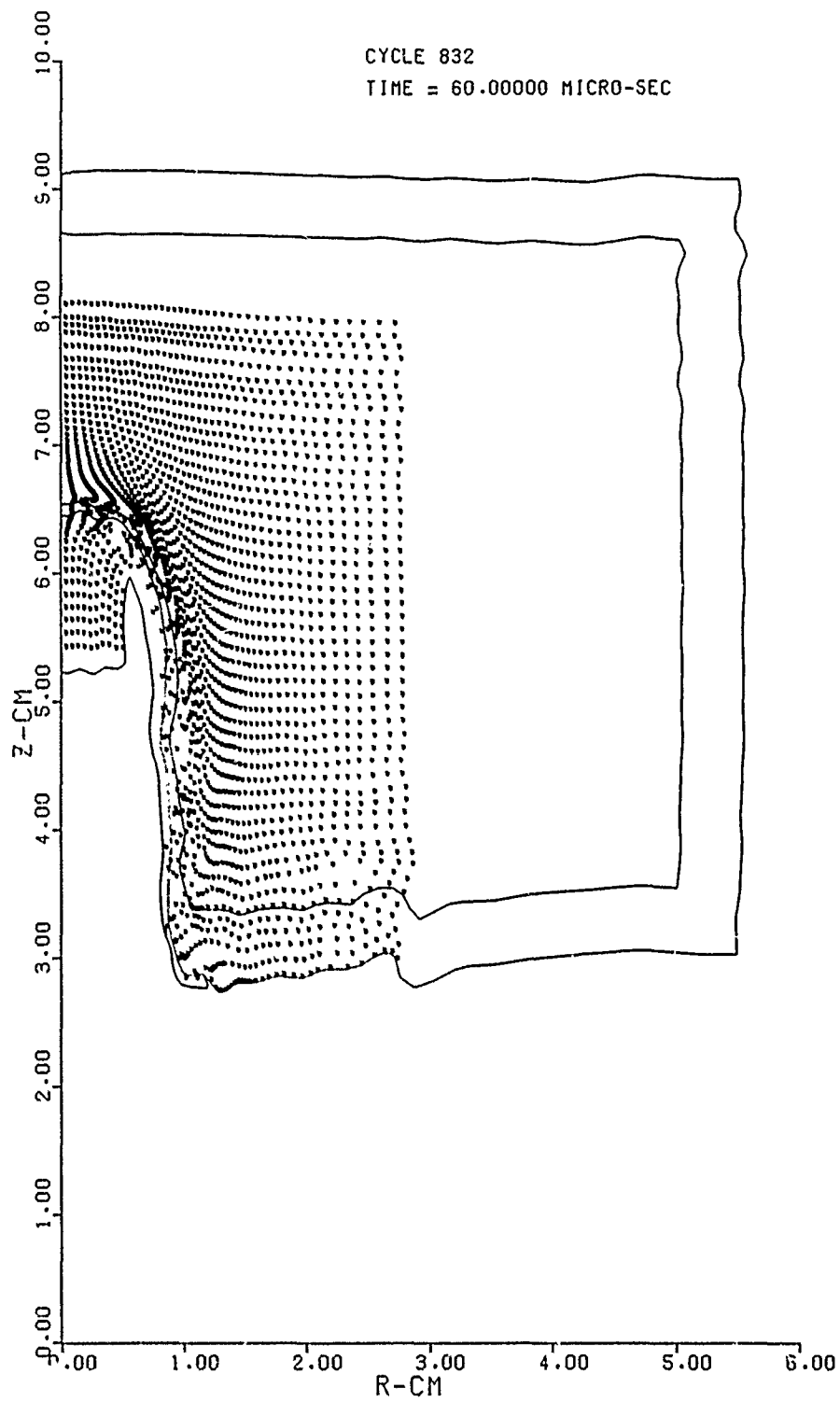


Figure 4. The Projectile/Explosive/Casing Configuration at $60 \mu\text{s}$ After the Impact for the Typical Case. (Impact Velocity = 1 km/s, Rad of Projectile = 0.5 cm)

COMPRESSION CYCLE= 832.0 TIME= 6.00000-05 SECONDS

			A	B	C	D	E	F	G	H
SIM3D-	.	-								
MAXIMUM VALUE	.468	.489	.510	.531	.552	.573	.594	.615	.636	.657
SIM3D-	I	J	K	L	M	N	O	P	Q	R
MAXIMUM VALUE	.678	.699	.720	.741	.762	.783	.804	.825	.846	.867
SIM3D-	S	T	U	V	W	X	Y	Z		
MAXIMUM VALUE	.888	.909	.930	.951	.972	.993	1.014	1.035		

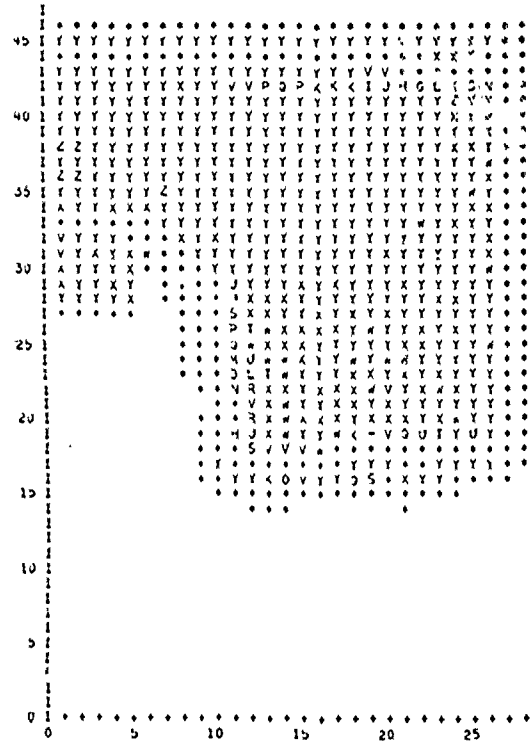


Figure 5. Compression Map at $60\mu s$ for the Typical Case.
 (Impact Velocity = 1 km/s, Rad of Projectile = 0.5 cm)

CYCLE 832

TIME = 60.00000 MICRO-SEC

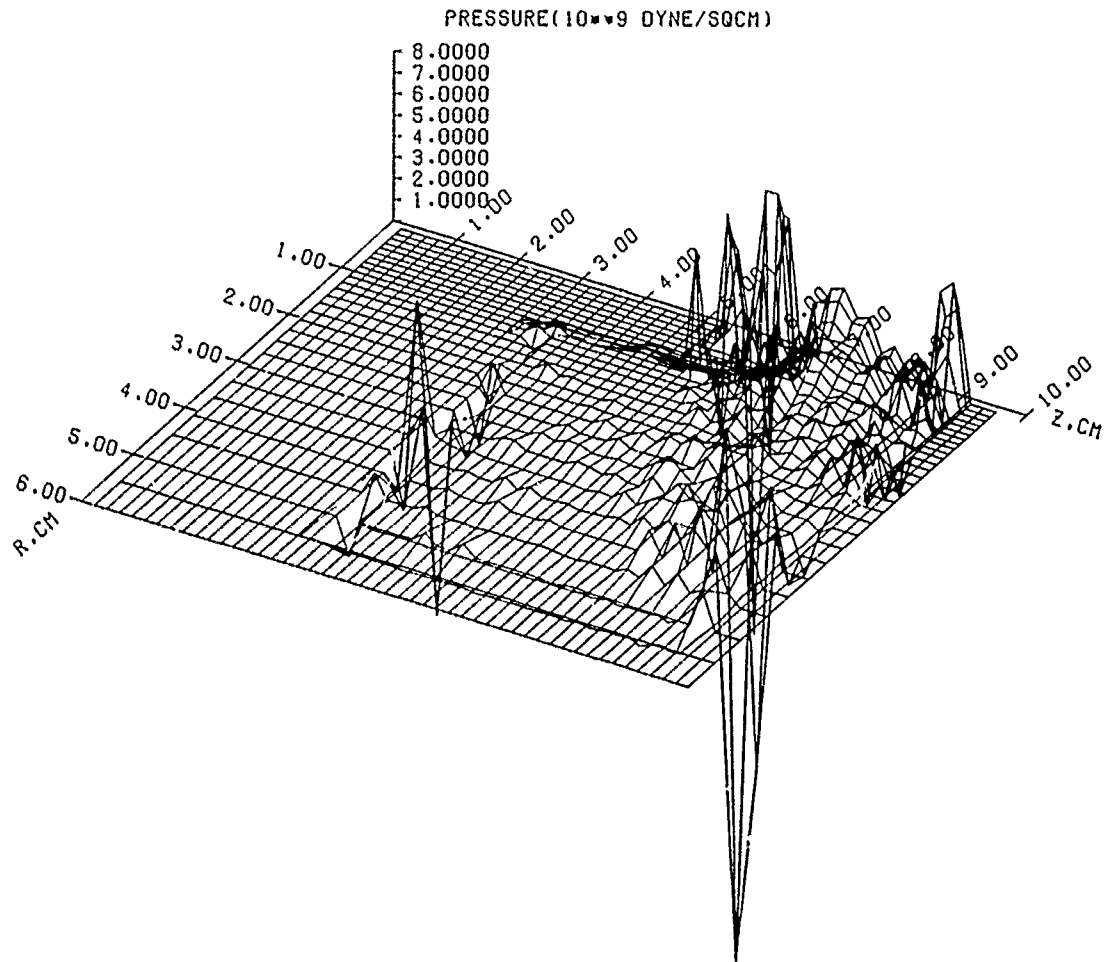


Figure 6. Pressure Map at 60 μ s for the Typical Case.
(Impact Velocity = 1 km/s, Rad of Projectile = 0.5 cm)

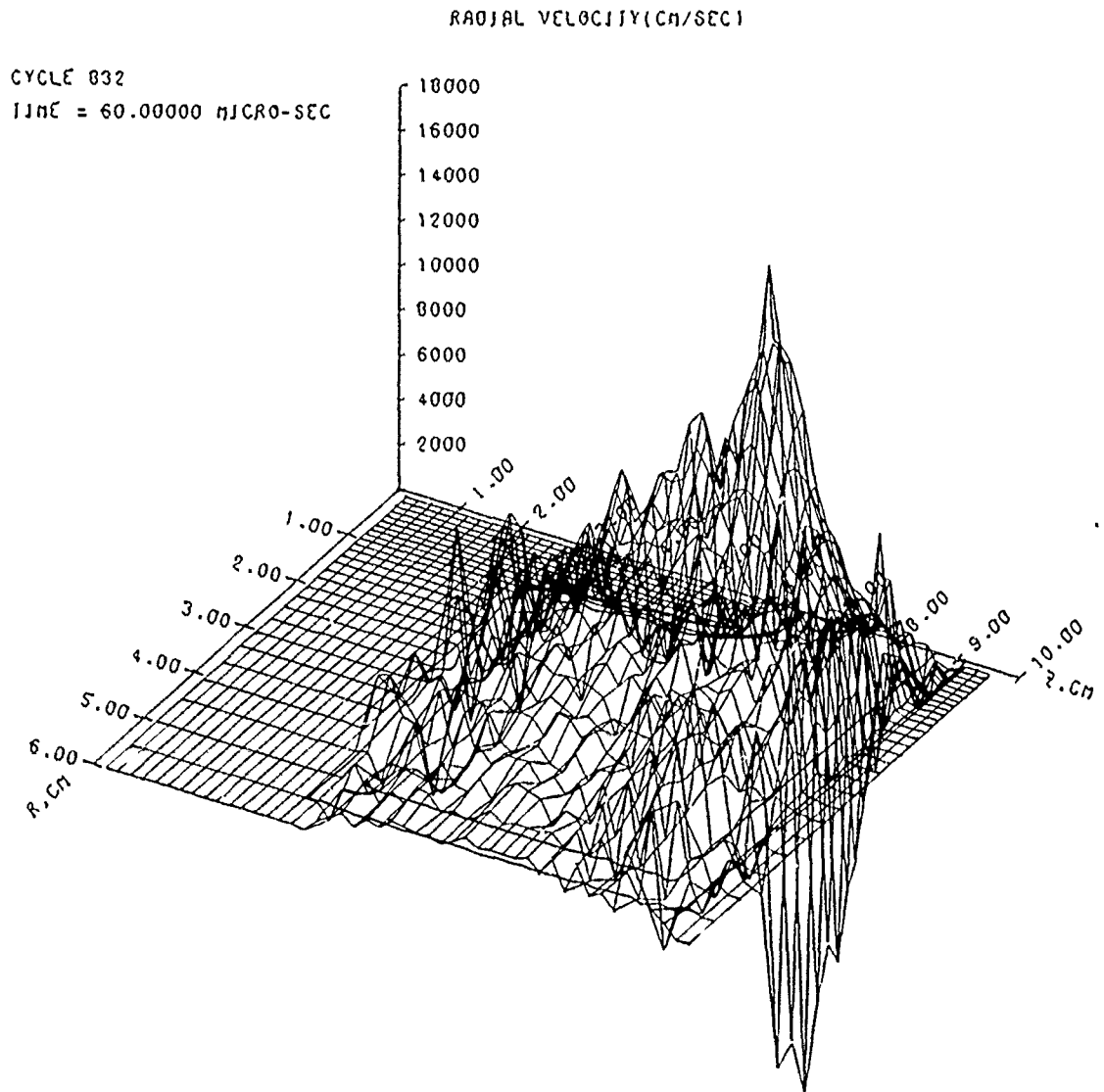


Figure 7. Radial Velocity Map at $60 \mu\text{s}$ for the Typical Case.
(Impact Velocity = 1 km/s, Rad of Projectile = 0.5 cm)

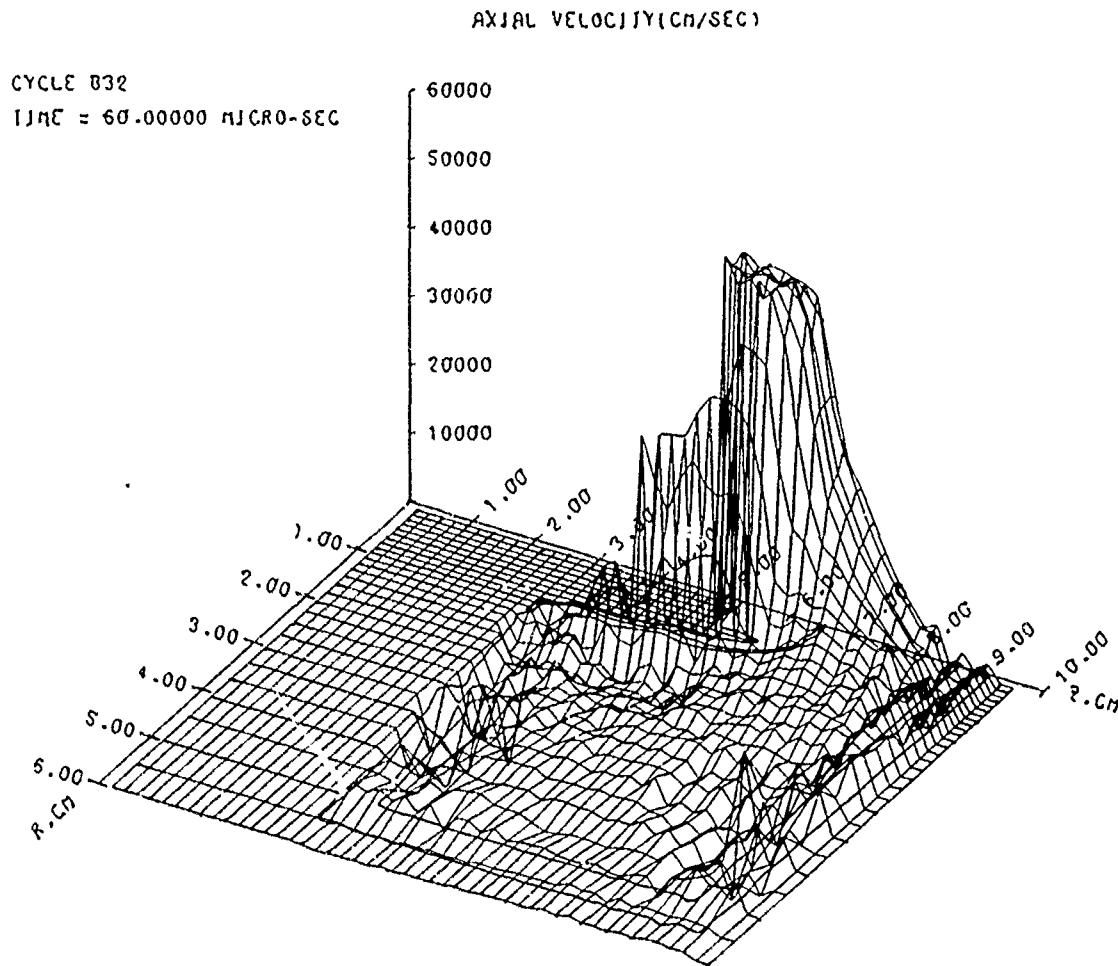


Figure 8. Axial Velocity Map at $60 \mu\text{s}$ for the Typical Case.

(Impact Velocity = 1 km/s, Rad of Projectile = 0.5 cm)

S. J. ENERGY (10¹⁰ ERG/GM)

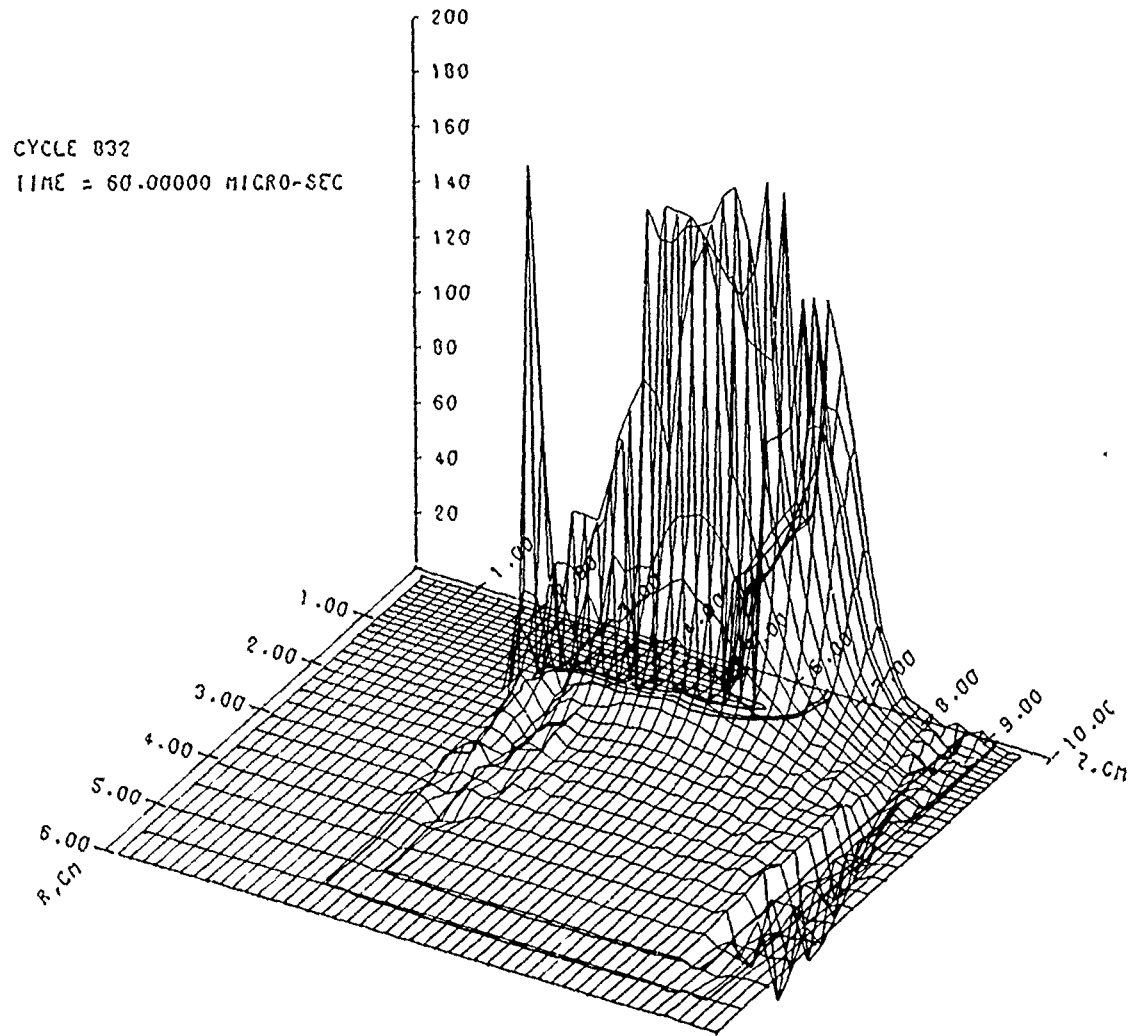


Figure 9. Specific Internal Energy Map at 60 μ s for the Typical Case.
(Impact Velocity = 1 km/s, Rad of Projectile = 0.5 cm)

150-107

HIGHEST TEMP OF THE CELL		CYCLE= 832.0 TIME= 6.00000E-05 SECONDS									
SYMBOL		A	B	C	D	E	F	G	H	I	J
MAXIMUM VALUE	0.00	7.50+01	7.50+00	1.50+01	2.25+01	3.00+01	3.75+01	4.50+01	5.25+01	6.00+01	6.00+01
SYMBOL	I	J	K	L	M	N	O	P	Q	R	S
MAXIMUM VALUE	6.75+01	7.50+01	8.25+01	9.00+01	9.75+01	1.05+02	1.12+02	1.20+02	1.27+02	1.35+02	1.35+02
SYMBOL	S	T	U	V	W	X	Y	Z			
MAXIMUM VALUE	1.42+02	1.50+02	1.57+02	1.65+02	1.72+02	1.80+02	1.87+02	1.95+02			

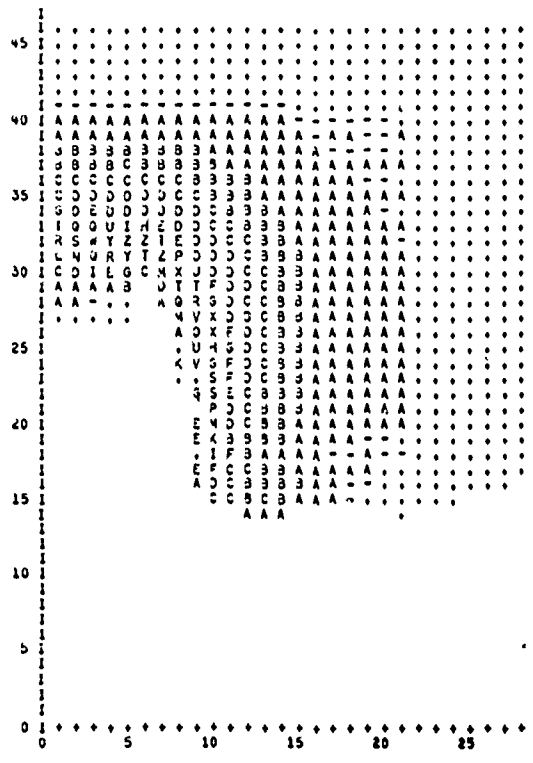


Figure 10. Map of the Highest Temperature of Cell at 60 μ s for the Typical Case.
 (Impact Velocity = 1 km/s, Rad of Projectile = 0.5 cm)

EXPLOSIVE HIGHEST TEMP	CYCLER 832.0				TIME= 6.00000-05 SECONDS				
SYMBOL	-	A	B	C	D	E	F	G	H
MAXIMUM VALUE	0.00	2.31+01	2.31+00	4.61+00	6.92+00	9.22+00	1.15+01	1.38+01	1.61+01
SYMBOL	I	J	K	L	M	N	O	P	Q
MAXIMUM VALUE	2.08+01	2.31+01	2.34+01	2.77+01	3.00+01	3.23+01	3.46+01	3.69+01	3.92+01
SYMBOL	S	T	U	V	W	X	Y	Z	
MAXIMUM VALUE	4.38+01	4.61+01	4.84+01	5.07+01	5.30+01	5.53+01	5.76+01	6.00+01	

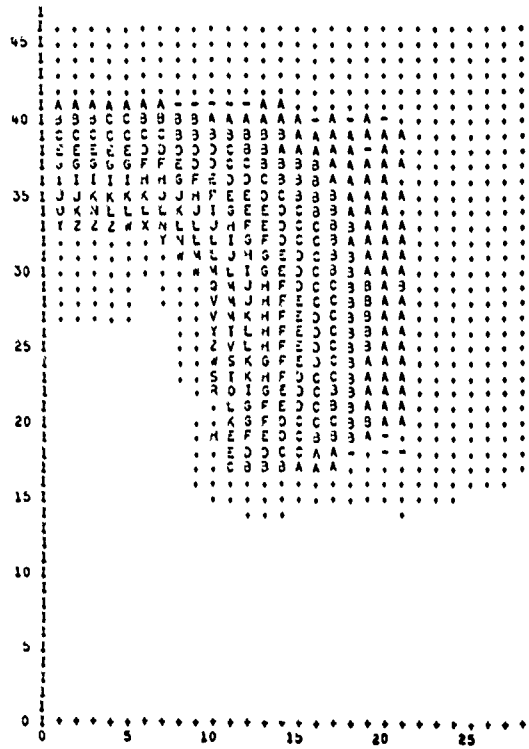


Figure 11. Map of the Highest Explosive Temperature of Cell at 60 μ s for the Typical Case.
(Impact Velocity = 1 km/s, Rad of Projectile = 0.5 cm)

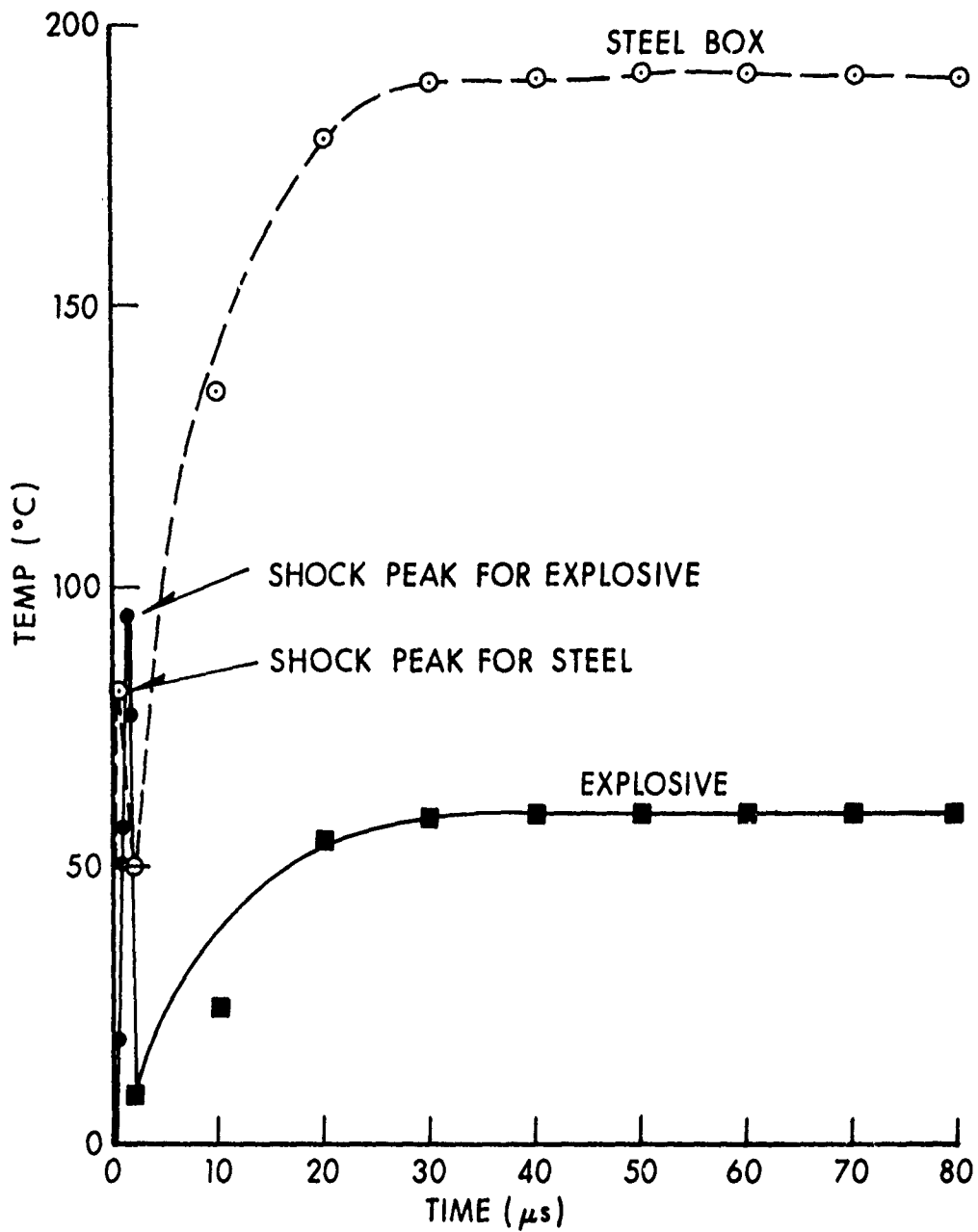


Figure 12. Plot of Temperature Rise of Steel and Explosive vs. Time for the Typical Case. (Impact Velocity = 1 km/s, Rad of Projectile = 0.5 cm)

(1) The highest shock temperature in the explosive is higher than the highest shock temperature in the metal. This is so because the explosive is more compressible than steel.

(2) More plastic work is done in the steel than in the explosive, because of the higher yield strength of the steel. At later times, the temperature in both materials would have been slightly higher if residual shock temperatures were taken into account.

(3) The highest plastic temperature in the explosive was associated with a tracer which was initially positioned adjacent to the metal interface. Even higher temperatures would have resulted if conduction from the metal were taken into consideration.

(4) Plastic work levels off in any material either because of tensile failure of the material or material melting. In the tensile failure case, both the hydrostatic and the deviatoric portions of the stress in the cells were zeroed out. The material near the crater lip usually fails in tension. Melting of the material is based on its specific internal energy acquiring a value equal to or greater than an inputted quantity 'melt energy'. According to equation (9), yield strength vanishes when the material melts. No additional plastic work can therefore be done on the material after it melts. In our calculation there is some evidence of explosive melting. The cell internal energies, however, always remained lower than the steel melt energy; tensile failure rather than melting was therefore the reason for plastic work leveling-off in the steel.

Figures 13 through 15 are plots of pressure versus time. In Figure 13, the pressure at the explosive/steel interface is plotted while in Figure 14 the pressure is plotted for the interface between the projectile and the steel box. In about 2 μ s, the pressure at the projectile interface drops to an insignificant level because of the relief waves arriving from the projectile free surface and the explosive interface. The pressure on the explosive/steel interface, on the other hand, remains significant for much longer time. The explosive near the interface first fails at about 10 μ s but heals soon after. At about 40 μ s, the crater lip is very well formed, material near the interface goes in tension and fails. The pressure throughout the sample drops to an insignificant level at this time, the failed material therefore cannot heal. The plastic temperature therefore does not change after 40 μ s. The highest grid pressure vs time is plotted in Figure 15. This figure illustrates the dissipation of shock inside the target.

B. Parametric Study

The test matrix shown in Table III was employed for investigating the effects of variation of impact velocity, projectile radius and casing thickness. In this study, the length of the projectile was always 2.0 cm.

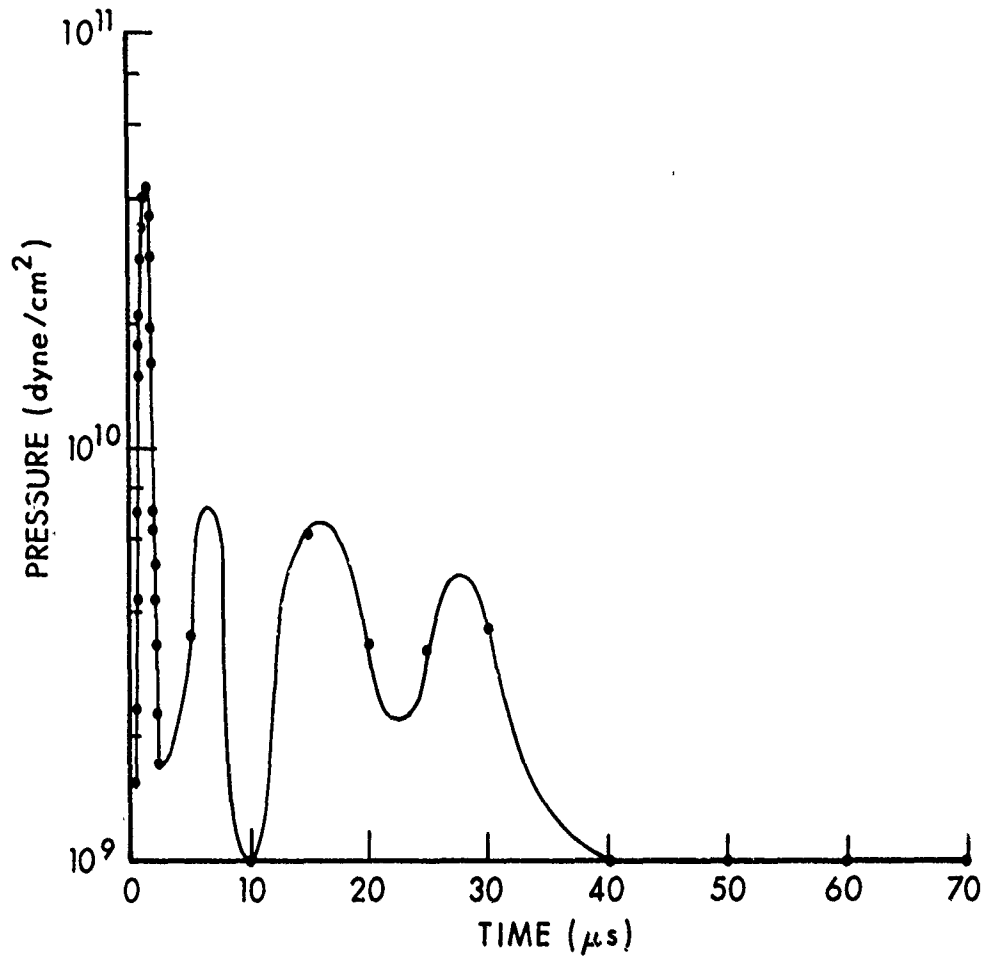


Figure 13. Pressure vs. Time Plot at the Explosive Interface for the Typical Case.
 (Impact Velocity = 1 km/s, Rad of Projectile = 0.5 cm)

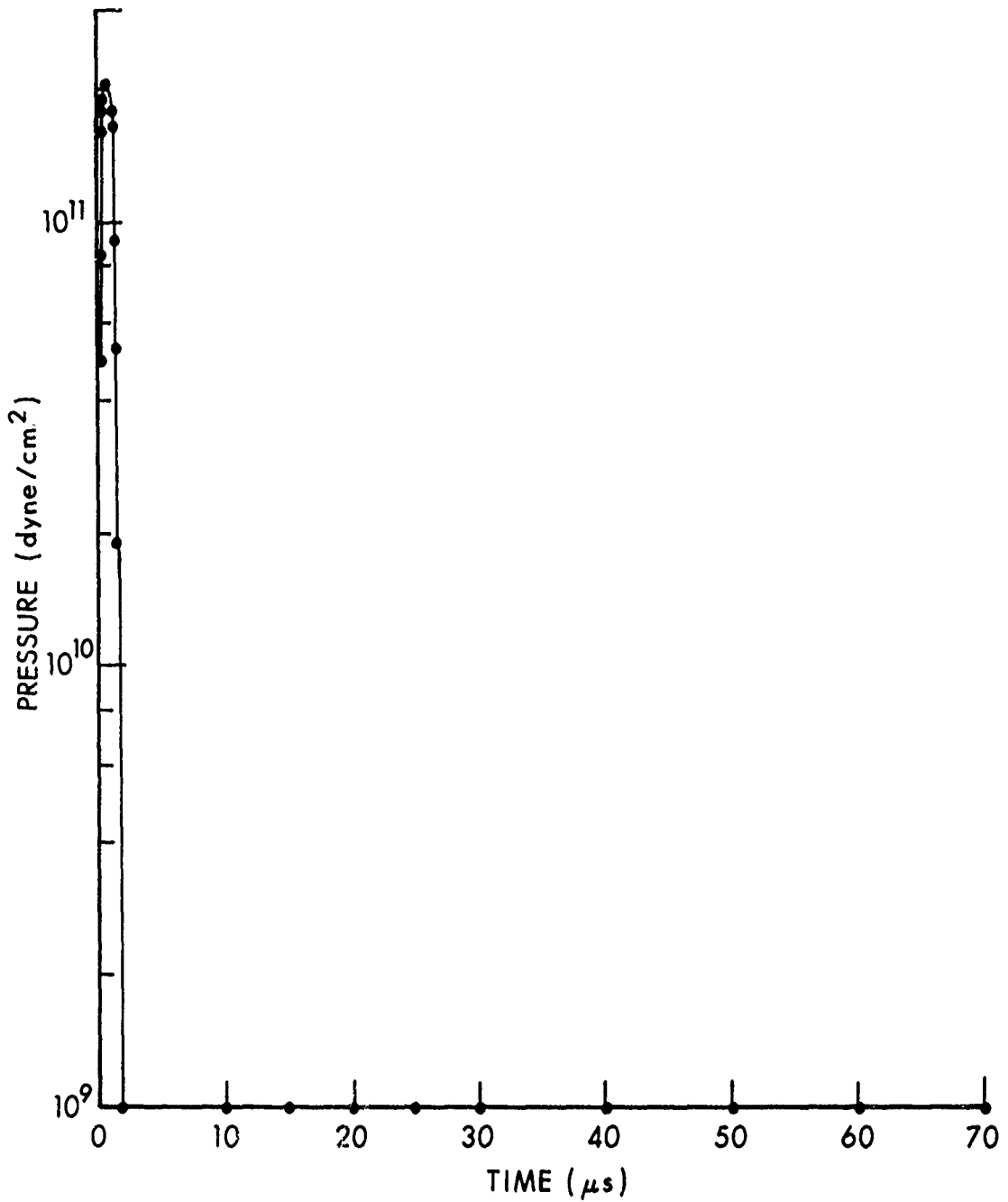


Figure 14. Pressure vs. Time at the Projectile/Casing Interface for the Typical Case.

(Impact Velocity = 1 km/s, Rad of Projectile = 0.5 cm)

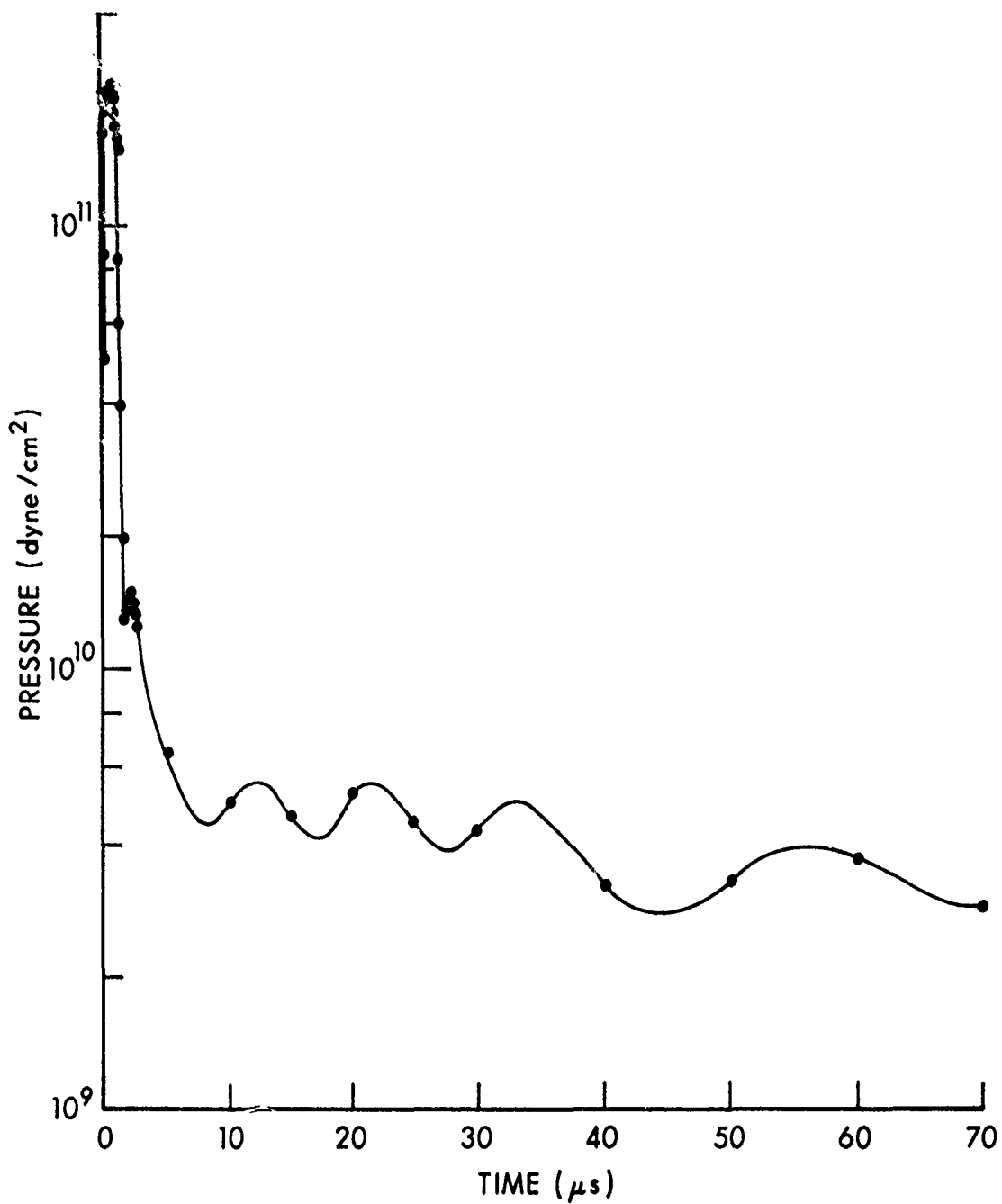


Figure 15. Dissipation of Shock Inside the Target for the Typical Case.
 (Impact Velocity = 1 km/s, Rad of Projectile = 0.5 cm)

Table III. The Test Matrix for the Parametric Study

$$\ell = 2.0 \text{ cm}$$

Calculation	Casing Thickness	Radius of Projectile	Impact Velocity	Residual Velocity
	d cm	r cm	v km/s	$v_{RES} = \frac{v}{1 + t/\ell}$ km/s
I	0.50	0.25	1.00	0.80
		0.50		
		1.00		
II	0.50	0.50	1.00	0.80
			2.00	1.60
			3.00	2.40
III	1.00	0.50	1.20	0.80

1. Effect of Projectile Size. Figure 16 shows the variation of plastic-work temperature with time in the explosive and the steel for three projectile radii, 0.25, 0.50 and 1.00 cm. Impact velocities for all the three cases were 1.0 km/s. It is clear from this plot that the dependence of the highest plastic work temperature, as well as its rise time, on the projectile diameter, is weak and complicated. Total plastic work for each of the material packages is, on the other hand, an increasing function of the projectile radius, as seen from Figure 17. As the projectile radius increases, bigger and bigger regions in the target are involved in the deformation process and acquire high temperatures. The probability of getting ignition due to plastic work therefore seems to be independent of projectile radius, as long as the fragment is large enough to insure plastic working of the explosive, but extent of the reaction may depend on radius. The numerical value of the highest temperature obtained in the explosive or the steel, however, does not change because the plastic work per unit volume does not.

Figure 18 is a plot of the highest explosive shock temperature versus projectile radius. The calculations indicate that the shock temperature increases rapidly as the projectile radius increases. However, the shock temperatures must plateau when the projectile radius is sufficiently great so that the shock reaching the explosive is planar. In the present calculations, this should have occurred at a radius of about 1 cm, and the failure of the calculations to reflect this must be due to the finite zone size.

2. Effect of Impact Velocity. Figure 19 is a plot of plastic work temperature in the explosive and the steel versus time for impact velocities, 1.0, 2.0, and 3.0 km/sec. The projectile radius for the three cases was 0.5 cm. It is clear from Figure 19 that the highest plastic-work temperature attained in either material is not strongly dependent on the projectile impact velocity in the range of values employed here. However, the plastic work temperature for the impact velocity of 3 km/s leveled at a much lower value because of an early tensile failure of the deformational regime. Since the plastic work has also been seen not to depend on the projectile radius, it can be concluded that the highest plastic work temperature is independent of projectile kinetic energy, as long as this energy is above a certain minimum value. Temperature ceases to rise after $t = 40 \mu\text{s}$ because of material failure in tension. Figure 20 is a plot of highest explosive shock temperature versus impact velocity. The explosive shock temperature increases as the impact velocity increases. For a given projectile kinetic energy, the variation in shock temperature is more dramatic with projectile velocity than with projectile radius.

3. Effect of Casing Thickness. One calculation was done using a casing thickness of $t = 1.0 \text{ cm}$, and impact velocity, $v = 1.2 \text{ km/s}$. The higher impact velocity was chosen so that the projectile residual velocity¹¹ be the same for the thicker casing as for the typical case

11. R. F. Recht and T. W. Ipson, *Trans ASME*, 85, 384, 1963.

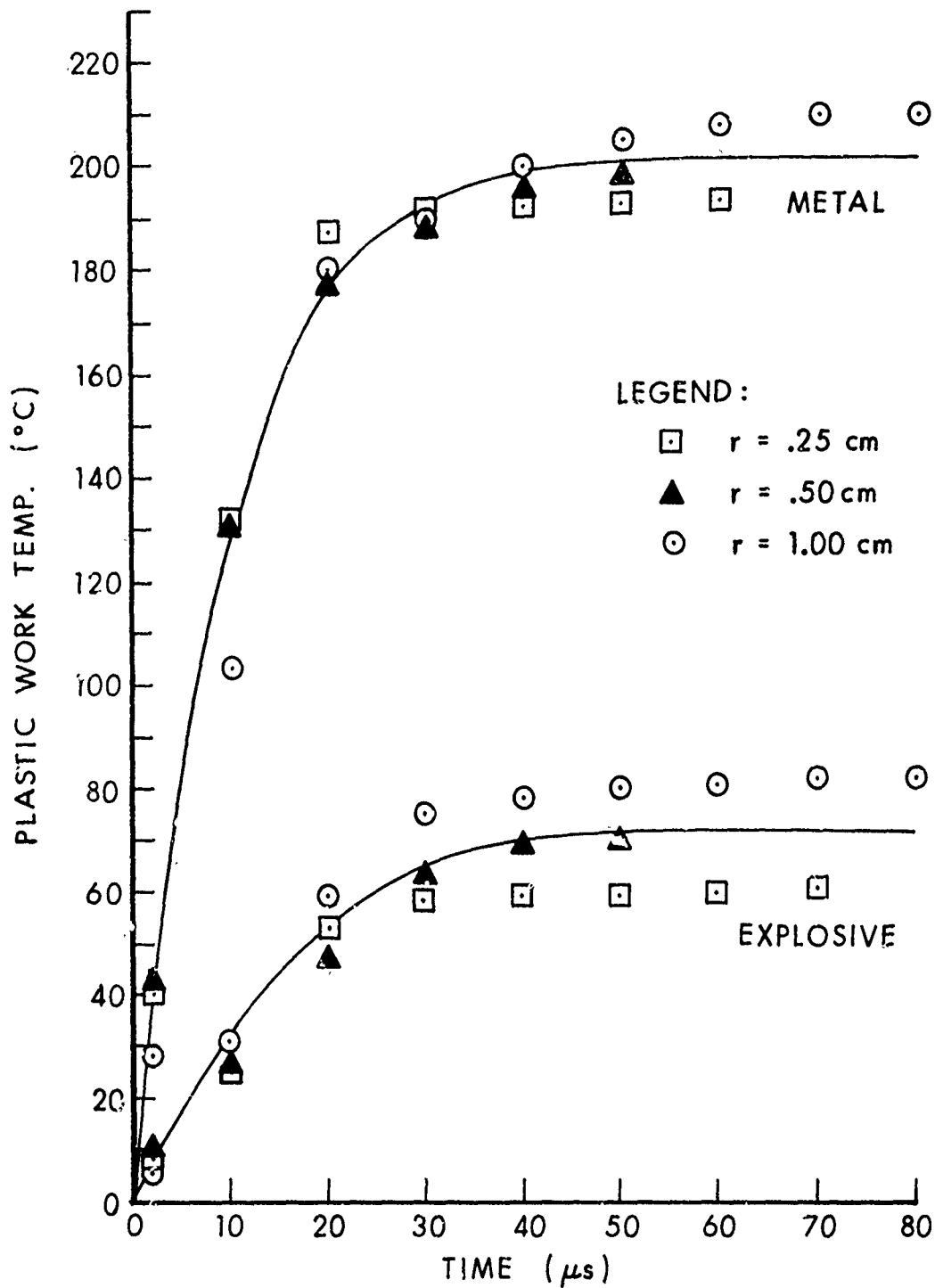


Figure 16. Metal and Explosive Plastic Work Temperatures vs. Time for $r = 0.25, 0.5, 1.0$ cm (Impact Velocity = 1 km/s)

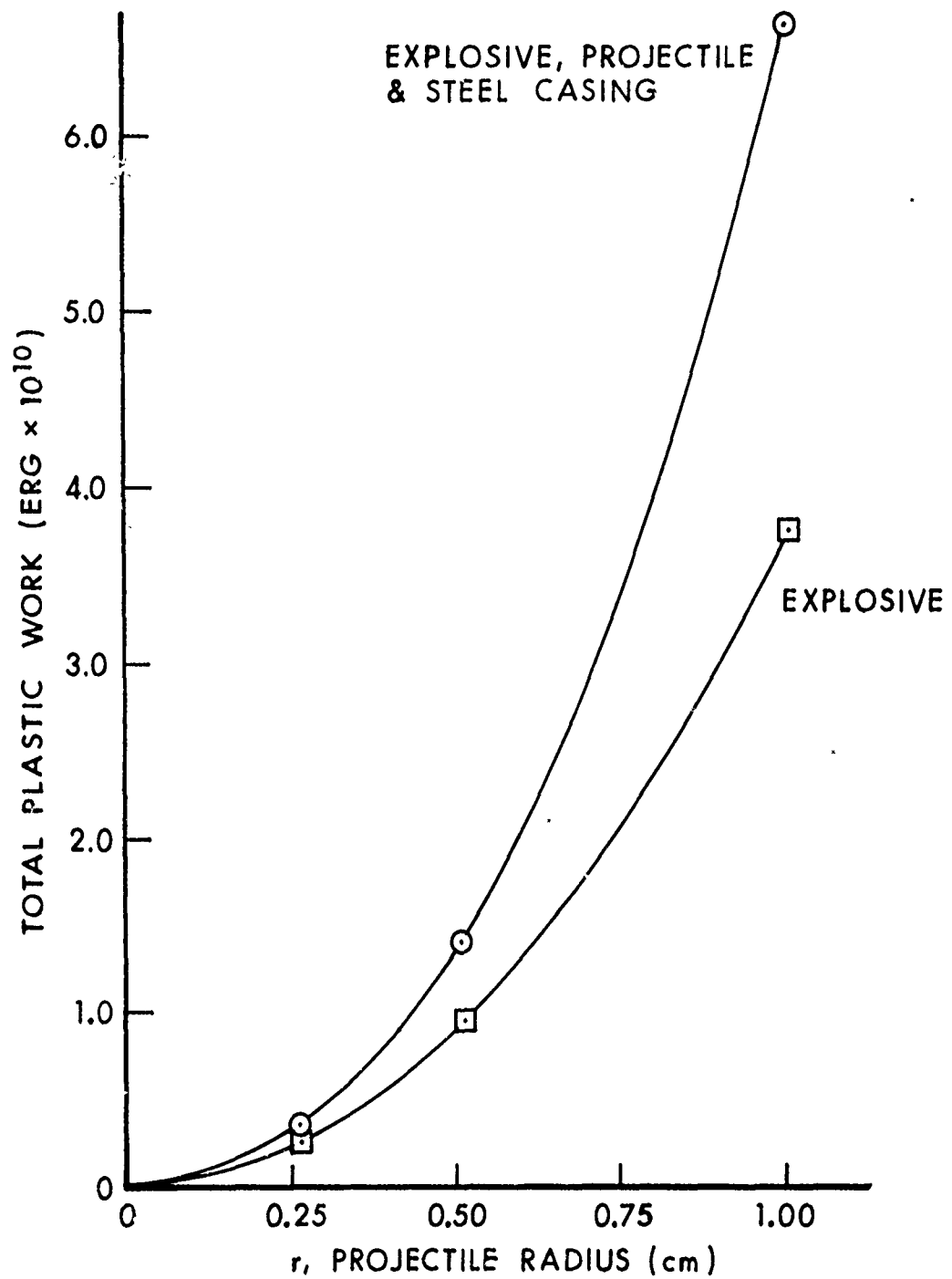


Figure 17. Total Plastic Work in Explosive vs. Projectile Radius at $t = 40 \mu\text{s}$

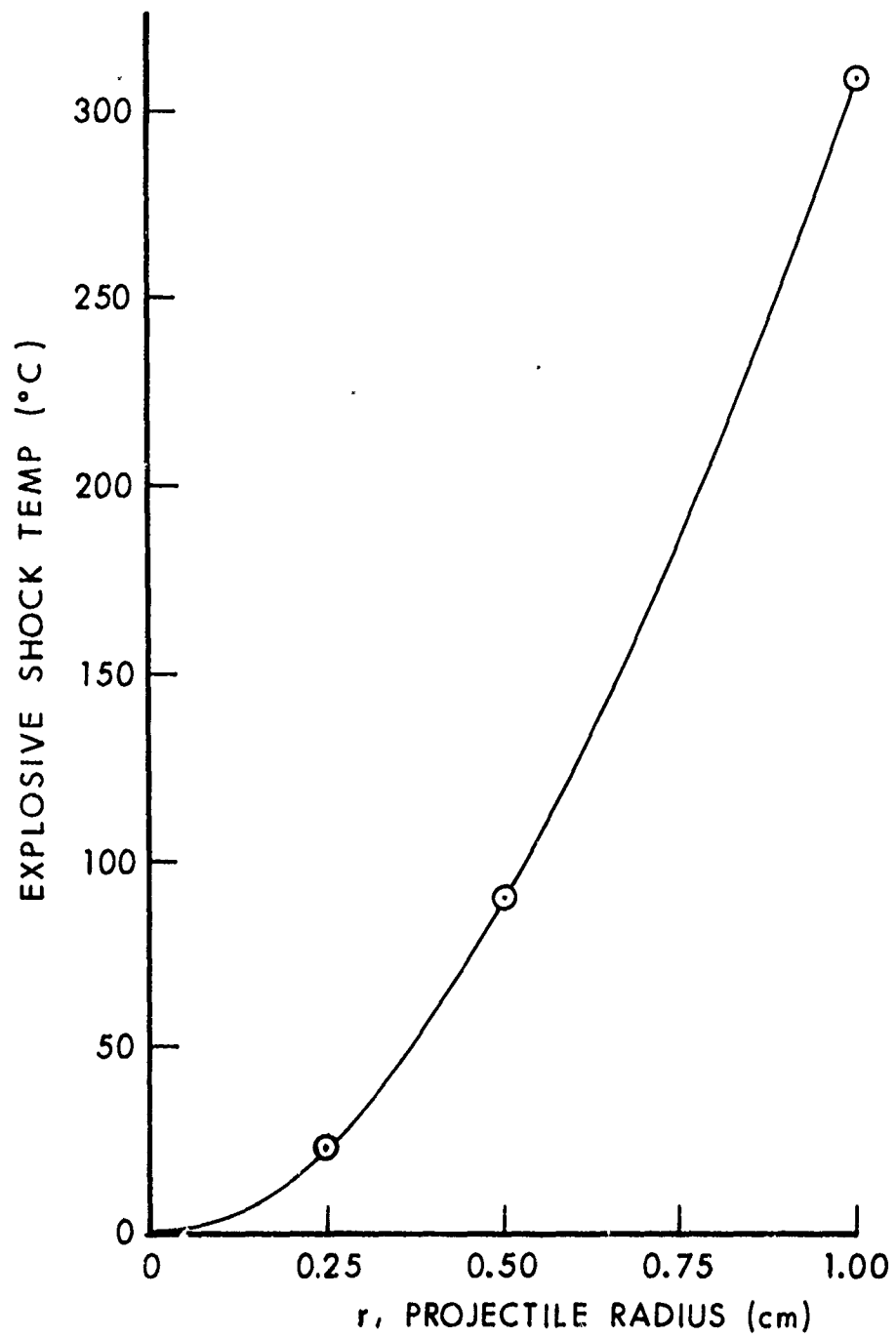


Figure 18. Explosive Shock Temperature vs. Projectile Radius (Impact Velocity = 1 km/s)

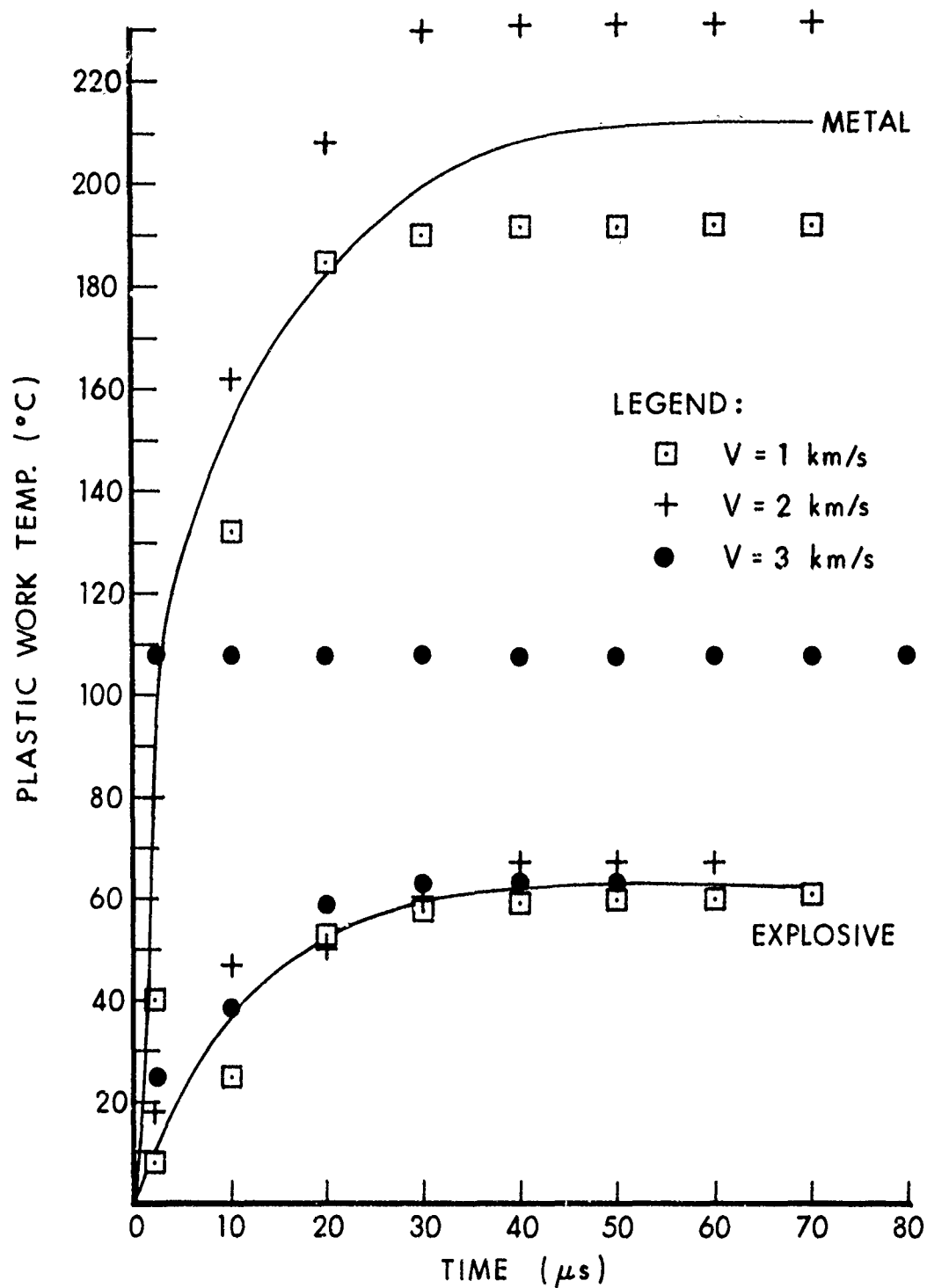


Figure 19. Metal and Explosive Plastic Work Temperatures vs. Time for $V = 1, 2, 3$ km/s (Projectile Radius = 0.5 cm)

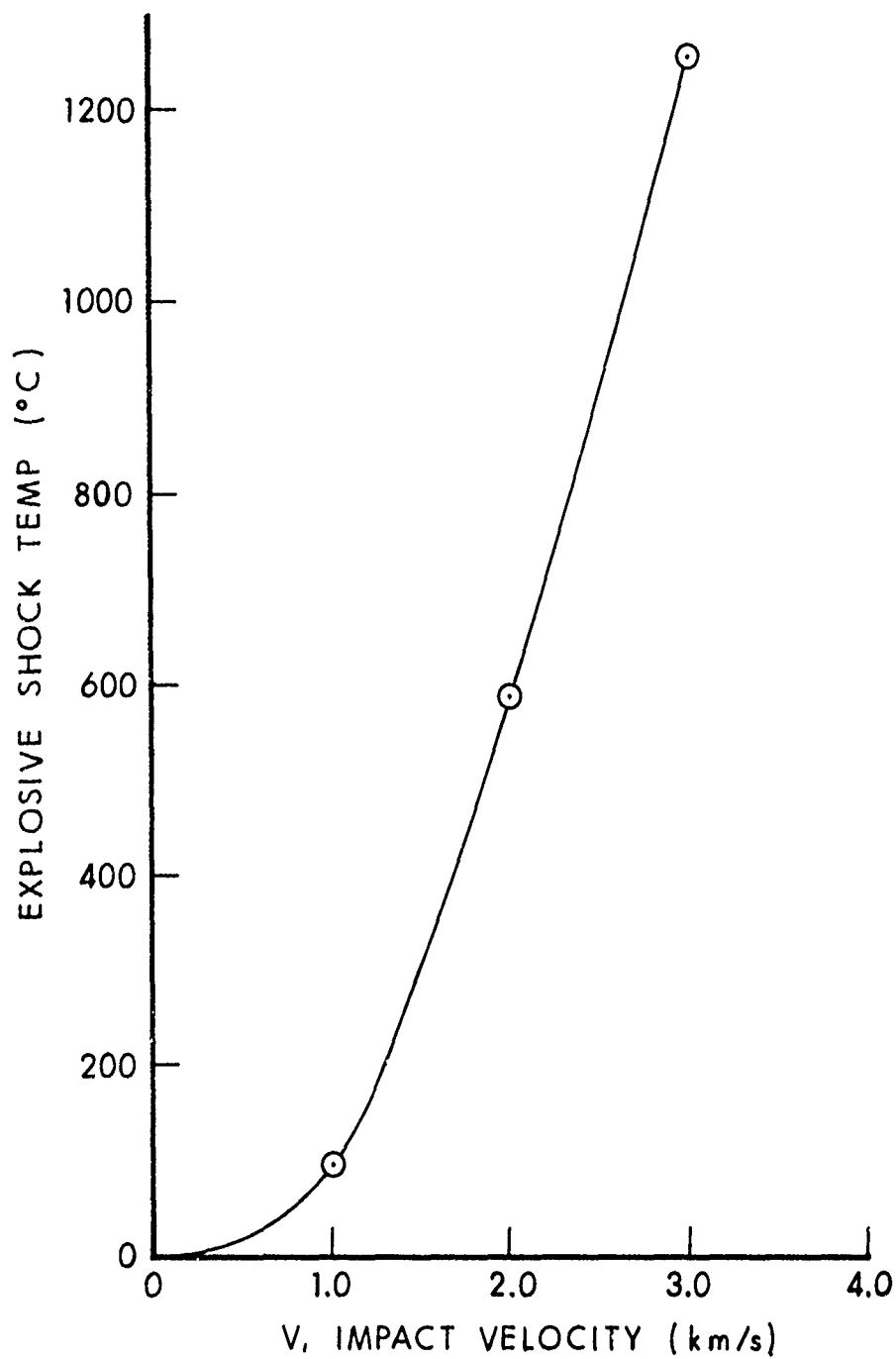


Figure 20. Explosive Shock Temperature vs. Projectile Velocity (Rad. of Projectile = 0.5 cm)

with $d = 0.5$ cm and $v = 1.0$ km/s. The highest shock temperature and the highest plastic work temperature are plotted as a function of the casing thickness in Figure 21, for both the explosive and the casing. Explosive shock temperature is seen to drop considerably as the casing thickness increases. Explosive plastic-work temperature, on the other hand, shows an increase with the increasing thickness which can be attributed to the delayed tensile-failure of the explosive when thicker casing is employed. The shock temperature in steel is slightly higher for the thicker casing, because of the higher impact velocity while its plastic work temperature is considerably higher, again because of its delayed tensile-failure.

C. Effect of Reduction of Cell Size

It is generally believed that the smaller the cell size, the greater is the accuracy of the computational results. In order to see the effect of reduction of cell size on the numerical value of the results, the cell size employed in the typical calculation was halved in the important deformation regime. It should be mentioned that the zone-size reduction is usually limited by the limited computer core and the rising cost of computation (core size is roughly inversely proportional to the square of the cell size). Care must be taken not to have cells in the grid whose aspect ratio is greater than two. If variable zoning is used, the zone size should change by no more than 10% from one cell to the next. Also, one should have no fewer than three cells, in order to describe a particular material dimension in the grid. Figure 22 is a plot of the explosive and the steel plastic-work temperatures versus zone size. Temperatures in both materials are seen to increase as the cell size decreases. It is felt that there may be a region near the axis which obtains very high strain. The code's ability to resolve such a region is limited due to the cell size in the radial direction, which has not been altered. The cell size in this calculation was halved by shortening its axial dimension.

If a linear extrapolation is assumed to be valid, one can easily calculate a plastic temperature rise of about 100°C in the explosive and about 400°C in the steel, for very small cell size. Since under the ambient conditions the explosive melts at about 80°C , a temperature higher than 80°C will be impossible for the explosive with the code unless viscous effects are included. The linear extrapolation for the explosive is therefore invalid, however an extrapolated temperature rise of 400°C for steel is quite interesting. It may mean that a temperature rise of 400°C , for the solid explosive in the neighborhood of the hot steel, is also possible. Local high temperature in steel will, however, be shortlived because of its high thermal conductivity.

D. Effect of High Tensile Strength

The bulk strain for material failure was decreased from $-.001$ to $-.1$ for the explosive and from $-.02$ to $-.1$ for the steel, in one of the calculations. The change, which was tantamount to increasing the

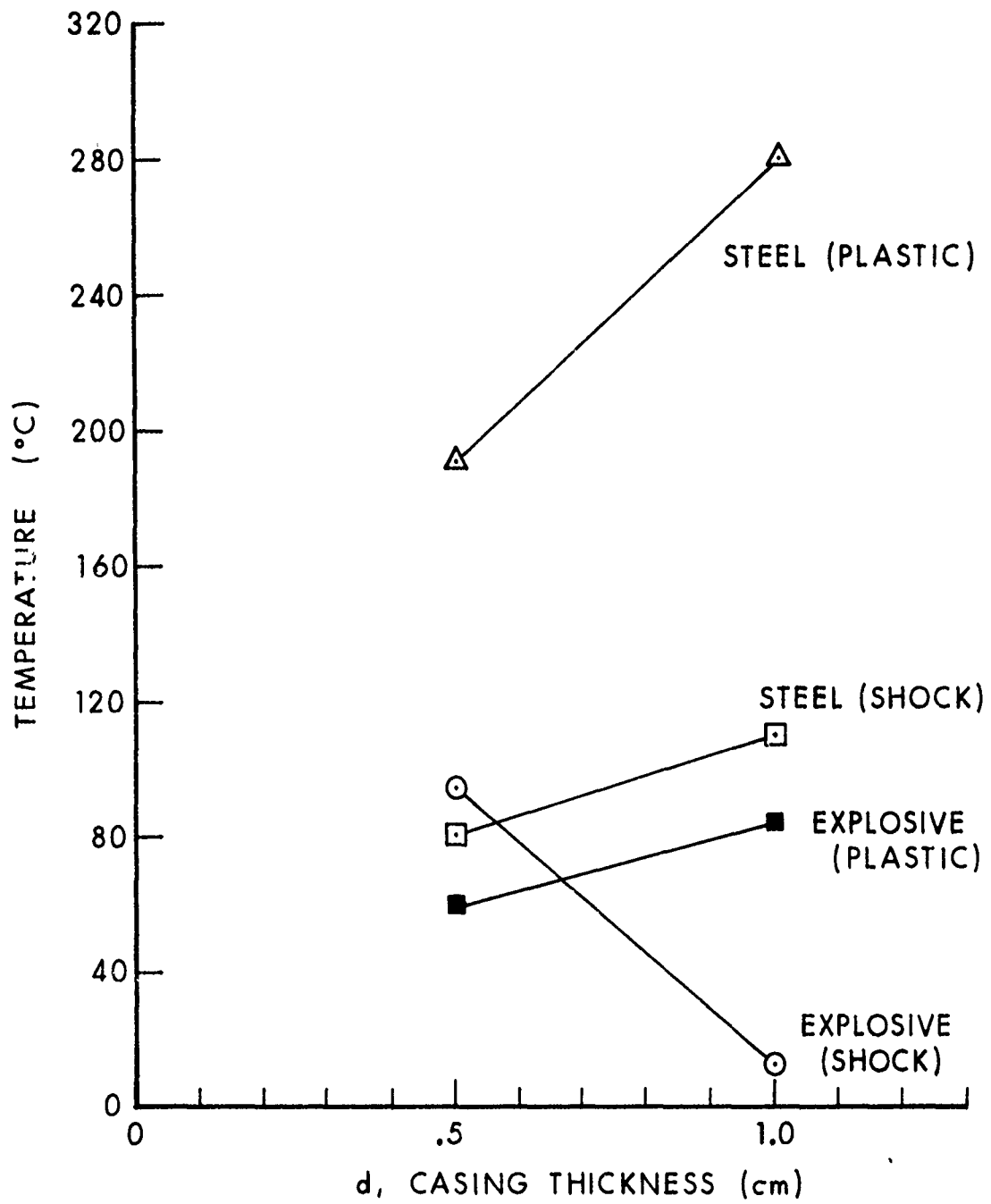


Figure 21. Metal and Explosive Temperatures vs. Casing Thickness

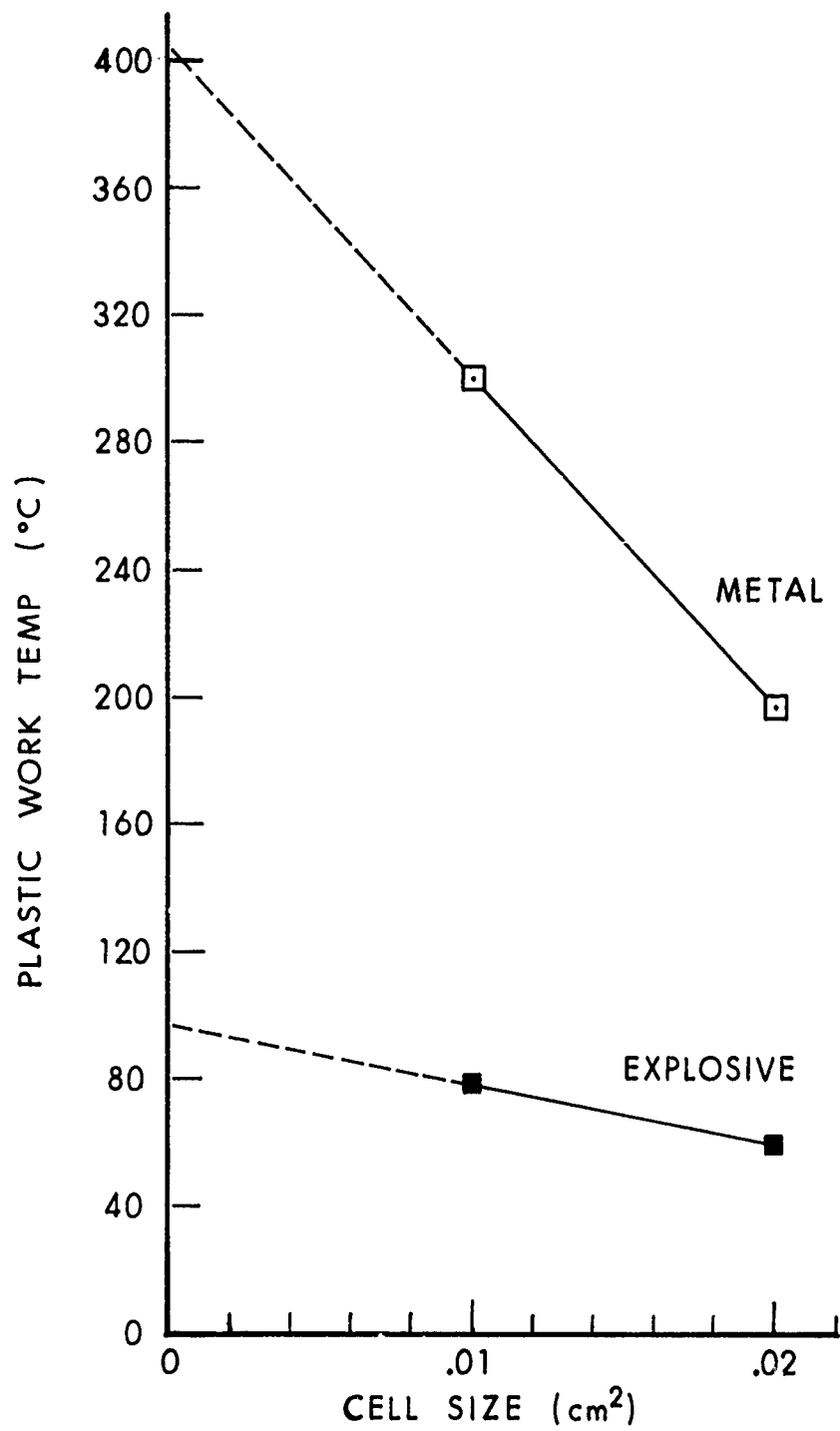


Figure 22. Metal and Explosive Plastic - Work Temperatures vs. Cell Size (Impact Velocity = 1.0 km/s, Rad of Projectile = 0.5 cm)

tensile strength of the material, did not noticeably alter the plastic-work temperature of the explosive. This indicates that the shear stresses were negligible at the time material failed in tension. The plastic work temperature would, of course, increase if the material yield strength were changed, which in turn indicates the significance of work hardening terms of equation (9).

E. Effect of Presence of Cracks or Notches in the Explosive Material

It is well known that crack tips act as stress-concentrators. The shear stress and the plastic work is therefore quite large at the crack tips. If the work hardening and the effect of pressure on melting point are disregarded, it follows that the highest plastic work temperature attainable at the stationary crack tip in explosive is 80°C, which is the melting point of the explosive. On the other hand, if there is any sliding between the cracked surfaces of the explosive material, it may be possible for the temperature to rise at the cracked explosive surface by frictional work since melting and heat conduction in the explosive are slow.

IV. CONCLUSIONS

Based on the results obtained from the numerical simulation of the normal impact of the confined explosives, one may conclude that:

- (1) Plastic work in explosive is limited by melting and tensile-failure.
- (2) Plastic work is dependent on the value chosen for the yield strength of the material. Work-hardening may play an important role in determining the plastic-work temperature.
- (3) If material failure in tension is disregarded, the highest plastic work temperature in explosive or steel is not too dependent on the projectile velocity or the projectile radius values employed in the numerical calculations here. For impact velocity of 3 km/s, however, the material failed in tension at a very early time.
- (4) The highest plastic work temperature in the explosive leveled off at about 40 μ s regardless of the projectile velocity and the projectile radius. At this time the crater lip was well formed and material in the vicinity of the lip failed in tension.
- (5) The highest shock temperatures in both steel and explosive are strongly dependent on the projectile radius and velocity.
- (6) Thicker confinement always lowers the explosive shock temperature but does not always alter the plastic deformation significantly. The plastic work thus may become relatively more important for the thicker casing.

(7) Explosive hot spots in the neighborhood of rapidly deforming steel casing may have a temperature of about 400°C. This deduction has been made by linearly extrapolating the plastic temperature versus cell size plot to the cell size of 0.0 cm².

(8) In addition to plastic deformation, heat conduction and friction between the grits or cracked surfaces of the explosive may also be important heating mechanisms in the explosives leading to violent reactions.

V. RECOMMENDATIONS FOR FUTURE WORK

A parametric study of the dependence of the explosive plastic-work on the projectile radius and the projectile velocity was attempted in this effort. This study ignored the viscous contribution to the stress-strain relation. Addition of this term might affect the results, particularly the dependence of plastic work on velocity. In addition, because of the strong sensitivity of the plastic-work temperature on the value of the yield strength, it is important to include the work-hardening and the thermal softening terms in the numerical computational scheme. Other important items that should be considered, in any calculations related to the explosive deformation, are the dependence of the melting point and the Grüneisen constant on pressure. Inclusions of failure modes other than the tensile mode should also be investigated and, if needed, incorporated in the numerical schemes. Frictional work may be an additional important heating mechanism in the explosives. The slide line concept employed in the plugging version of HELP code may be useful in studying the relative material motion leading to viscous heating of a small layer of the explosive which has just melted inside a narrow crack in the explosive.

ACKNOWLEDGMENTS

Indebtness is acknowledged to Dr. Philip M. Howe for holding numerous enlightening discussions. Ms. Laura J. Hageman and Dr. Robert T. Sedgwick provided a copy of the latest version of the HELP computer code along with invaluable consultation. Ms. Toni M. Taylor and Messers. John J. Misey, George H. Jonas, John T. Harrison and Alvin L. Arbuckle helped with the programming aspect of this study. A special note of thanks is due to Ms. Sandra Rosinski for her fast and accurate typing.

REFERENCES

1. S. N. Heavens and J. E. Fields, Proceedings of the Royal Society, A338, 77, 1974.
2. G. T. Afanasev and V. K. Bobolev, "Initiation of Solid Explosives by Impact," U.S. Department of Commerce, Springfield, VA, 1971.
3. H. A. Napadensky, "Initiation of Explosives by Low Velocity Impact," Fourth Symposium on Detonation, U.S. Naval Ordnance Laboratory, White Oak, MD, 1965.
4. C. A. Kot, H. A. Napadensky, Y. A. Shikari, and A. H. Wiedermann, "A Numerical Study of Impact Phenomena in Explosives and Propellants," Proceedings of the International Conference on Computational Methods in Nonlinear Mechanics, University of Texas, Austin, TX, 1974.
5. S. Brown and E. Whitbread, Les Ondes de Detonation, 1961.
6. J. Dewey and D. Slade, BRL Report 1021, 1957.
7. R. Frey, G. Melani, M. Chawla, and J. Trimble, "Initiation of Violent Reactions by Projectile Impact," Sixth Symposium on Detonation, San Diego, CA, 1976.
8. L. J. Hageman, D. E. Wilkins, R. T. Sedgwick and J. L. Waddell, "HELP: A Multi-Material Eulerian Program for Compressible Fluid and Elastic-Plastic Flows in Two Space Dimensions and Time," Systems, Science & Software Report No. SSS-R-75-2654, 1975.
9. R. T. Sedgwick, J. L. Waddell, M. Baker and J. M. Walsh, "Studies of Erosion and Impact Resistance of ABM Materials," BRL Contract Report No. 301, 1976.
10. J. M. Walsh and R. H. Christian, Phys Rev, 97, 1544, 1955.
11. R. F. Recht and T. W. Ipson, Trans ASME, 85, 384, 1963.

APPENDIX A. EQUATION OF STATE OF COMP B3

In order to study the shock wave propagation in materials, a relationship between the equilibrium thermodynamic state parameters, P, V and E is required. Such a relationship is called "Equation of State". Many different forms of these relationships are available in literature; Gray, Tillotson or Mie-Grüneisen type equations of state are more suitable for describing the thermodynamical state of a solid explosive, such as Comp B3.

In this report an equation of the Mie-Grüneisen type has been used. This equation was calibrated by employing an experimental Hugoniot. In addition, the Grüneisen parameter was assumed to be a constant. A Hugoniot typically defines all the pressure-volume states obtainable through a shock transition. Usually the Hugoniot of material is available in the form of experimental data points consisting of shock velocity and particle velocity. Usage of Rankine-Hugoniot jump conditions reduces the above data to equivalent data consisting of pressure and volume (or compression). Following sections illustrate the derivation of a Mie-Grüneisen equation of state for Comp B3 starting from the shock wave data.

A. Shock Wave Data

N. L. Coleburn and T. P. Liddiard* first reported the shock wave data for Comp B3 which is reproduced in Table A-I.

This experimental data was subjected to a least square curve fit yielding the following relationship between the shock velocity and the particle velocity.

$$U_s = 2.66 + 1.92 U_p \text{ (km/s)} \quad (\text{A-1})$$

Equation (A-1) expresses the material shock velocity as a linear function of the particle velocity. The constant term in equation (A-1) has the significance of sound speed, c_0 . Equation (A-1) also expresses the fact that the sound speed is the lowest value a shock can acquire. Ideally a material subjected to a plane shock undergoes no lateral deformation. Each macroscopic volume element is compressed exactly as its lateral neighbors and is therefore deformed only in the direction of the shock propagation. In reality the material develops a shear and if the yield stress is exceeded, plastic flow takes place in the material on a microscopic scale. As a result, the stress of the material cannot just consist of isotropic hydrostatic pressure, but will have a shear component as well. In the experiments, however, only the normal component of the stress is usually measured, the shear has to be inferred from the material constitutive relationship.

* N. L. Coleburn and T. P. Liddiard, *J. Chem. Phys.*, 44, 1929, 1966.

Table A-I. Shock Wave Data for Comp B3 ($\rho_0 = 1.68$)

U_s	U_p
km/s	km/s
3.387	0.380
3.437	0.421
3.439	0.469
3.510	0.466
3.628	0.462
3.713	0.460
3.971	0.741
4.243	0.819
4.314	0.886
4.346	0.869
4.377	0.884
4.441	0.936
4.469	0.881

The basic equations used in the study of shock are obtained by straightforward application of the conservation of mass, momenta and energy across a shock front. Assumption is made here that the initial and the final states are equilibrium states. In Figure A-1, a shock moving into the material at rest, with a velocity, U_s , produces a particle velocity, U_p , and raises the pressure from P_o to P_H , the density from ρ_o to ρ_H , and the specific internal energy from E_o to E_H .

The Rankine-Hugoniot relationships expressing the conservation laws are

$$\rho_o U_s = \rho_H (U_s - U_p) \quad (A-2)$$

$$P_H - P_o = \rho_o U_s U_p \quad (A-3)$$

$$E_H - E_o = \frac{1}{2} (P_H + P_o) (V_H - V_o) \quad (A-4)$$

Equations (A-2) and (A-3) can be rearranged to yield expressions for pressure and compression,

$$P_H = \rho_o U_s U_p \quad (A-5)$$

$$\mu_H \equiv \frac{\rho_H}{\rho_o} - 1 = \frac{U_p}{U_s - U_p} \quad (A-6)$$

where the initial pressure P_o has been neglected. Equation (A-1) can now be used to eliminate U_p from equations (A-5) and (A-6), yielding

$$P_H = \frac{\rho_o U_s (U_s - 2.66)}{1.92} \quad (A-7)$$

and

$$\mu_H = \frac{U_s - 2.66}{0.92 U_s + 2.66} \quad (A-8)$$

For a given shock speed, equations (A-7) and (A-8) yield a data point. A number of such data points are obtained for shock velocities in the range $c_o \leq U_s \leq 3c_o$. These values can be fitted to a polynomial of the form

$$P_H = F\mu_H + G\mu_H^2 \quad (A-9)$$

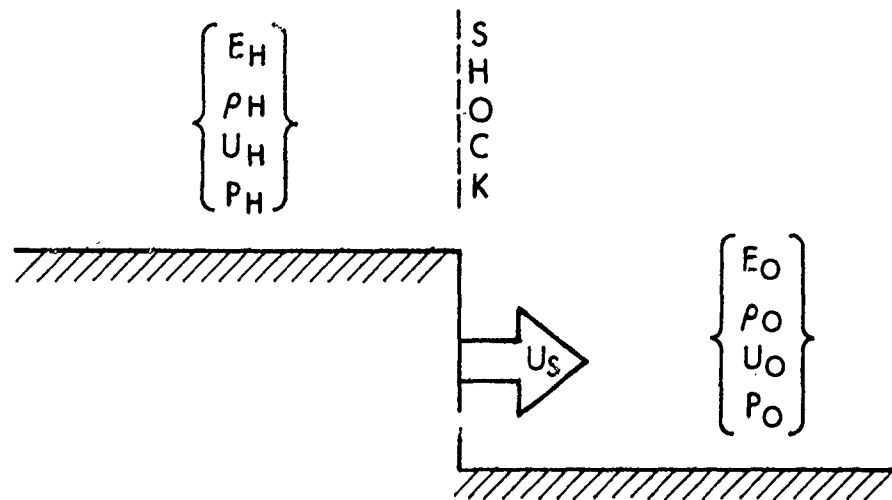


Figure A1. A Plane, One-Dimensional Shock Wave

Equation (A-9) gives the value of \bar{p} for any Hugoniot shock compression state, μ_H . Once the pressure, P_H , is determined from equation (A-9), the Hugoniot energy can simply be obtained from equation (A-4).

B. Mie-Grüneisen Equation of State

A Hugoniot state characterized by P_H (or μ_H) and E_H can now be used as a ready reference for determining all the possible material states. These states may not necessarily be reached by a plane shock compression. Such states may arise in a real material, where the finite dimensions of the sample will give rise to rarefactions or in the case where the impacting projectile and the resulting shock are non-planar. In these cases, lateral deformations are not negligible. A convenient equation of state is of the Mie-Grüneisen type:

$$P - P_H = \frac{\Gamma(V)}{V} (E - E_H) \quad (A-10)$$

where $\Gamma(V)$ is a Grüneisen parameter, P , V and E are any equilibrium pressure, volume and energy. An expression for the Grüneisen parameter is obtained by differentiating equation (A-10),

$$\Gamma(V) = V \left(\frac{\partial P}{\partial E} \right)_V = \frac{V}{C_V} \left(\frac{\partial P}{\partial T} \right)_V \quad (A-11)$$

Usually the Grüneisen parameter is a weak function of volume, its volume dependence will, therefore, be ignored. On substituting equation (A-4) into (A-10), one obtains

$$P = P_H \left(1 - \frac{\Gamma\mu}{2} \right) + \Gamma\rho E \quad (A-12)$$

where $\rho = 1/V$ is the density of the material corresponding to pressure P and energy E . On substituting the expression for P_H from the polynomial fit of equation (A-9) into (A-12), one obtains

$$P = (A\mu + B\mu^2 + C\mu^3) + \Gamma\rho E \quad (A-13)$$

where A , B , C are constants given by:

$$\begin{aligned} A &= 13.5 \times 10^{10} \\ B &= 9.5 \times 10^{10} \text{ (dyne/cm}^2\text{)} \\ C &= 100.6 \times 10^{10} \end{aligned} \quad (A-14)$$

Equation (A-13) is a general equation of state used to describe the response of Comp B3 under dynamic loading. Figure A-2 is a schematic showing the relationship between the equilibrium thermodynamic parameters, P, V and E. In Figure A-2, a shock hydrostat is shown along with a few pressure-volume curves with constant energies.

It should be pointed out that equation (A-13) is valid strictly for the compressed states, i.e. for $\mu > 0$. The $\mu < 0$ values correspond to expanded states of material, for which the hydrostatic pressure must become tensile. In order to ensure this behavior from an equation of state, it is customary to change the sign of the square term in equation (A-13). The resulting curve is shown in Figure A-3. Comp B3 fails for small negative pressure, Appendix B indicates that Comp B3 fails for $\mu \leq -.001$.

It is generally assumed that a Mie-Grüneisen type equation of state is adequate for metals in the low pressure regime, $P < 10$ kbar. Typical peak pressures obtained in impacts involving confined explosives are usually less than 50 kbar. The suitability of Mie-Grüneisen equation to describe the explosive behavior is, however, still an open question.

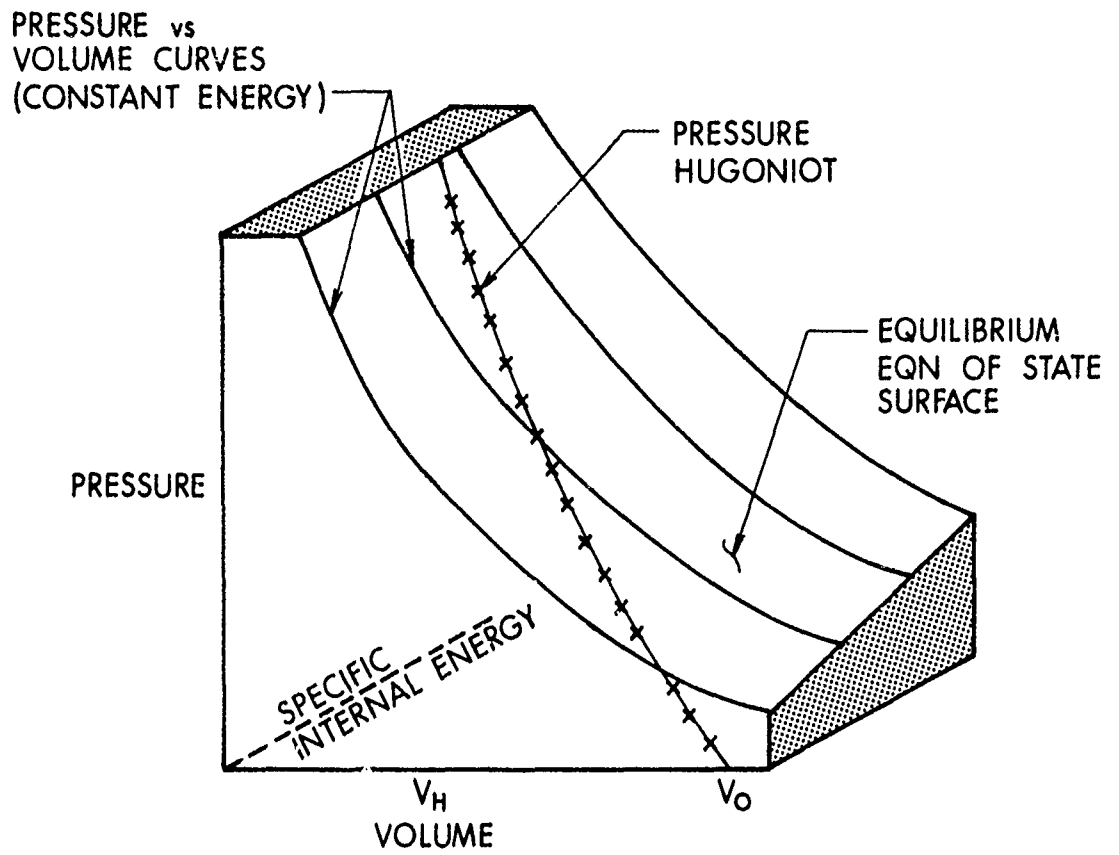
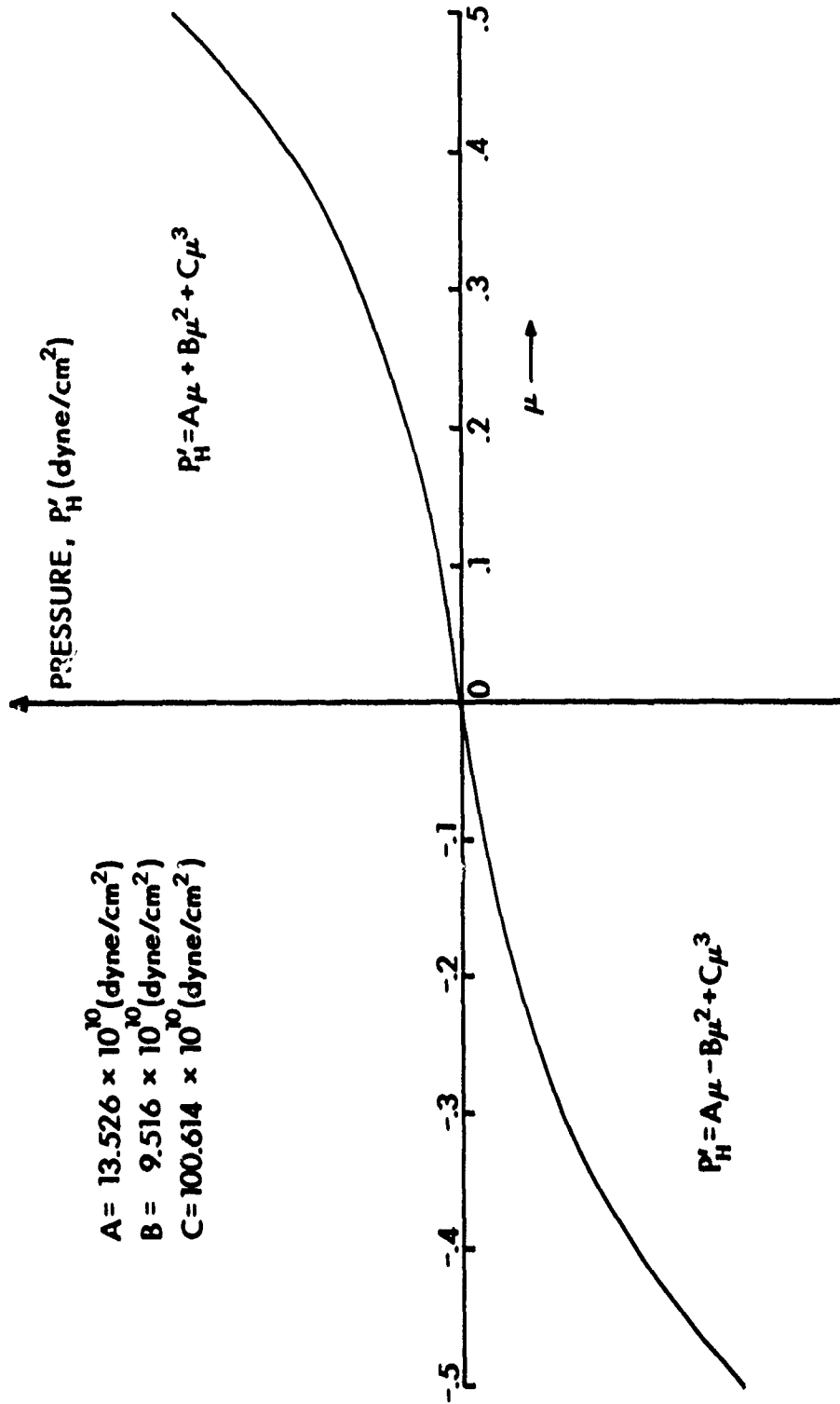


Figure A2. Equation of State Surface



$A = 13.526 \times 10^{10}$ (dyne/cm²)
 $B = 9.516 \times 10^{10}$ (dyne/cm²)
 $C = 100.614 \times 10^{10}$ (dyne/cm²)

Figure A3. Curve fit of the Hugoniot pressure of Comp B3

APPENDIX B. MATERIAL CONSTANTS FOR COMP B3

This section lists the values of miscellaneous parameters that are usually needed as input for a computational work involving Comp B3. These values have been collected from several sources. In the present computational work, the parameters of the explosive, PBX 9404 were employed if the corresponding parameters for Comp B3 were not readily available.

MISC CONSTANTS

$$\text{Density, } \rho_0 = 1.68 \text{ g/cm}^3$$

$$\text{Coefficient of friction, } \mu = .35$$

$$\text{Critical shock initiation energy, } \frac{p_t^2}{\rho U_s} = 29 \text{ cal/cm}^2$$

SOUND VELOCITIES

$$\text{Longitudinal shear velocity, } C_L = \sqrt{\frac{\kappa + \frac{4}{3}G}{\rho}} = 3.15 \times 10^5 \text{ cm/s}$$

$$\text{Transverse shear velocity, } C_S = \sqrt{\frac{G}{\rho}} = 1.73 \times 10^5 \text{ cm/s}$$

$$\text{Bulk sound speed, } c_b = \sqrt{\frac{\kappa}{\rho}} = 2.44 \times 10^5 \text{ cm/s}$$

ELASTIC CONSTANTS

$$\text{Bulk Modulus, } \kappa = \rho_0 c_b^2 = 10.037 \times 10^{10} \text{ dyne/cm}^2$$

$$\text{Shear Modulus, } G = \rho_0 c_s^2 = 5.029 \times 10^{10} \text{ dyne/cm}^2$$

$$\text{Poisson's ratio, } \nu = \frac{3\kappa - 2G}{2(G + 3\kappa)} = .29$$

$$\text{Hugoniot elastic limit, } H_{EL} = 1.5 \text{ kb (PBX 9404)}$$

$$\text{Tensile yield stress, } Y_T = \left(\frac{1 - 2\nu}{1 - \nu}\right) H_{EL} = 0.88 \text{ kb}$$

$$\text{Shear yield stress, } Y_S = \frac{1}{3} Y_T = 0.51 \text{ kb}$$

Ultimate tensile strength, $S = .1042 \text{ kb}$

Volumetric strain for failure, $\mu_{\text{MIN}} = -\frac{S}{K} = -.001$

Maximum distension for failure, $\text{AMDM} = \mu_{\text{MIN}} + 1 = .999$

THERMAL PROPERTIES

Normal melting temperature, $T_{\text{MELT}} = 80^{\circ}\text{C}$

Energy required to melt, $E_m = J C_v T_{\text{MELT}} = 1.13 \times 10^9 \text{ erg/g}$

Specific heat, $C_v = \begin{cases} .299 \text{ at } 30^{\circ}\text{C} \\ .307 \text{ at } 50^{\circ}\text{C} \\ .325 \text{ at } 70^{\circ}\text{C} \\ .333 \text{ at } 83^{\circ}\text{-}100^{\circ}\text{C} \end{cases}$

Thermal conductivity, $k = 6.27 \times 10^{-4} \text{ cal/cm-sec-}^{\circ}\text{C}$

Coefficient of thermal expansion, $\alpha = 54.6 - 97.5 \times 10^{-6} \text{ cm/cm-}^{\circ}\text{C}$

Grüneisen constant, $\Gamma = \left(\frac{\partial P}{\partial E}\right)_v = 0.947$

APPENDIX C. WALSH-CHRISTIAN TECHNIQUE

Temperature rise due to shock compression of metals along a Hugoniot and subsequent temperature drop of the material along an adiabat can be easily calculated by simple application of thermodynamics. The thermodynamical identity,

$$T dS = C_V dT + \left(\frac{\partial P}{\partial T}\right)_V T dV \quad (C-1)$$

The Rankine-Hugoniot jump condition,

$$E_H - E_0 = \frac{1}{2} (P_H + P_0) (V_0 - V_H) \quad (C-2)$$

and the second law of thermodynamics,

$$T dS = dE + P dV \quad (C-3)$$

form a starting point for such a calculation. The derivation of an appropriate expression was given by Walsh and Christian¹⁰ several years ago and is presented here for the sake of completeness.

From equations (C-1), (C-2) and (C-3), it is easily seen that the energy, along a Hugoniot, is not an independent variable and can therefore be eliminated. This is accomplished by first integrating equation (C-3) and then substituting equation (C-2) for the energy terms. The result is

$$\int_{S_0}^{S_H} [T dS]_{HUG} = \frac{1}{2} (P_H + P_0) (V_0 - V_H) + \int_{V_0}^{V_H} [P dV]_{HUG} \quad (C-4)$$

Integration of equation (C-1) yields

$$\int_{S_0}^{S_H} [T dS]_{HUG} = C_V (T_H - T_0) + \int_{V_0}^{V_H} \left(\frac{\partial P}{\partial T}\right)_V T dV \quad (C-5)$$

Differentiating equations (C-4) and (C-5) and equating the right hand sides of equations (C-4) and (C-5) eliminates the entropy terms as well. The result is

$$C_V \left(\frac{d T_H}{d V_H}\right) + \left(\frac{\partial P_H}{\partial T}\right)_{V_H} T_H = f(V_H) \quad (C-6)$$

where

$$f(V) = \frac{1}{2} P + \frac{1}{2} \frac{dP}{dV} (V_0 - V) \quad (C-7)$$

Further simplification of equation (C-6) results by assuming that C_v and $(\frac{\partial P}{\partial T})_v$ are constants. The resulting equation is a nonhomogeneous, first order differential equation

$$\frac{d T_H}{d V_H} + b T_H = \frac{f(V_H)}{C_v} \quad (C-8)$$

where

$$b = \frac{(\partial P / \partial T)_v V_H}{C_v} \quad (C-9)$$

The solution of equation (C-8) is easily obtained to be

$$T_H = T_0 e^{b(V_0 - V_H)} + e^{-bV_H} \int_{V_0}^{V_H} \left[\frac{f(V) e^{bV}}{C_v} dV \right]_{HUG} \quad (C-10)$$

The second term on the right hand side of equation (C-10) can be expressed in terms of Hugoniot parameters; A, B, C [Equation (1)]. The result is

$$T_H = T_0 e^{b(V_0 - V_H)} + \frac{1}{2} \frac{V_0}{C_v} e^{-bV_H} \int_0^{\mu_H} \frac{(A + B)\mu^2 + 2(B + C)\mu^3 + 3C\mu^4}{(1 + \mu)^2} e^{\frac{bV_0}{1+\mu}} d\mu \quad (C-11)$$

The integral in equation (C-11) can be evaluated analytically but is obtained here numerically in order to save time. It should be mentioned that in this work, only the peak temperature obtained by explosive during the shock is of concern. However, soon after the passage of the shock wave, material begins to release itself along an adiabat. The temperature of the material as a consequence of this adiabatic expansion, drops. The temperature corresponding to any volume attained by the material during this expansion is easily calculated from equation (C-1), where dS is set equal to zero. The resulting equation is

$$C_v dT + \left(\frac{\partial P}{\partial T}\right)_v T dV = 0 \quad (C-12)$$

The solution to this is given by

$$T_{AD}(V_{AD}) = T_H e^{b(V_H - V_{AD})} \quad (C-13)$$

Normally, V_{AD} is the inverse of density of the material under full compaction. Equations (C-11) and (C-13) give a complete temperature history of the material undergoing a shock compression and subsequent adiabatic expansion. Because of the irreversible nature of the shock, both the energy and temperature of the system are higher after the passage of the shock, the residual temperature being given by:

$$T_{RES} = T_{AD} - T_0 \quad (C-14)$$

LIST OF SYMBOLS

<u>Symbol</u>	<u>Definition</u>	<u>Units*</u>
AMDM	compression for tensile failure of material	--
b	Γ/V	cm^{-3}
c_o	sound speed	km/s
C_v	specific heat at constant volume	cal/g-°C
d	casing thickness	cm
E	specific internal energy	erg/g
E_H	Hugoniot specific internal energy	erg/g
E_m	melt energy per unit mass	erg/g
J	mechanical equivalent of heat	erg/cal
P	pressure	dyne/cm ²
P_H	Hugoniot pressure	dyne/cm ²
r	projectile radius	cm
s_{ij}	deviatoric stress	dyne/cm ²
S	spall strength	dyne/cm ²
t	time	S
T	temperature	°C
T_o	initial temperature	°C

* The CGS system of units is employed here in order to be consistent with the input/output of the HELP code.

<u>Symbol</u>	<u>Definition</u>	<u>Units</u>
u_j	velocity	cm/s
U_p	particle velocity behind the shock	km/s
U_s	shock velocity	km/s
v	impact velocity of the projectile	km/s
v_{Res}	residual projectile velocity	km/s
V	specific volume	cm^3
V_0	initial specific volume	cm^3
W	specific plastic work	erg/g
Y	yield strength	dyne/cm^2
Γ	Grüneisen constant	--
ϵ_{ij}	strain	--
n	ρ/ρ_0	--
κ	bulk modulus	dyne/cm^2
σ_{ij}	stress	dyne/cm^2
μ	$\rho/\rho_0 - 1$	--

DISTRIBUTION LIST

<u>No. of Copies</u>	<u>Organization</u>	<u>No. of Copies</u>	<u>Organization</u>
12	Commander Defense Documentation Center ATTN: DDC-TCA Cameron Station Alexandria, VA 22314	2	Commander US Army Missile Research and Development Command ATTN: DRDMI-R DRDMI-RBL Redstone Arsenal, AL 35809
1	Director Defense Advanced Research Projects Agency ATTN: Tech Info 1400 Wilson Boulevard Arlington, VA 22209	1	Commander US Army Tank Automotive Development Command ATTN: DRDTA-RWL Warren, MI 48090
1	Director Defense Nuclear Agency ATTN: MAJ T. Stong Arlington, VA 22209	4	Commander US Army Mobility Equipment Research & Development Command ATTN: Tech Docu Cen, Bldg. 315 DRSME-RZT Dr. J. Bond Mr. D. Dinger Fort Belvoir, VA 22060
1	Commander US Army Materiel Development and Readiness Command ATTN: DRCDMA-ST 5001 Eisenhower Avenue Alexandria, VA 22333	1	Commander US Army Armament Materiel Readiness Command ATTN: DRSAR-RDT, Dr. T. Hung Rock Island, IL 61202
1	Commander US Army Aviation Systems Command ATTN: DRSAV-E 12th and Spruce Streets St. Louis, MO 63166	5	Commander US Army Armament Research and Development Command ATTN: SARPA-AD-EP Mr. V. Guadagno Mr. T. Stevens Mr. A. Fiorentino Dr. D. Weigand Dover, NJ 07801
1	Director US Army Air Mobility Research and Development Laboratory Ames Research Center Moffett Field, CA 94035		
2	Commander US Army Electronics Command ATTN: DRSEL-RD DRSEL-HL-CT Mr. S. Crossman Fort Monmouth, NJ 07703	1	Commander US Army Rock Island Arsenal ATTN: SARRI-LA-AC, W. Wells Rock Island, IL 61201

DISTRIBUTION LIST

<u>No. of Copies</u>	<u>Organization</u>	<u>No. of Copies</u>	<u>Organization</u>
2	Commander US Army Frankford Arsenal ATTN: SARFA-FCA-W Mr. D. Swartz SARFA-MDA-A Mr. D. Donnelly Philadelphia, PA 19137	1	Deputy Assistant Secretary of the Army (R&D) Department of the Army Washington, DC 20310
1	Commander US Army Watervliet Arsenal ATTN: SARWV-RDD-SE Mr. P. Vottis Watervliet, NY 12189	1	HQDA (DAMA-ARP) Washington, DC 20310
1	Commander US Army Harry Diamond Labs ATTN: DRXDO-TI 2800 Powder Mill Road Adelphi, MD 20783	1	HQDA (DAMA-MS) Washington, DC 20310
5	Commander US Army Materials and Mechanics Research Center ATTN: DRXMR-T, J. Bluhm DRXMR-T, Dr. Roylance DRXMR-T, Dr. Wilde Dr. Mescall DRXMR-ATL Watertown, MA 02172	1	Commander US Army Research Office ATTN: Dr. E. Saibel P. O. Box 12211 Research Triangle Park NC 27709
1	Commander US Army Natick Research and Development Command ATTN: DRXRE, Dr. E. Sieling Natick, MA 01761	1	Chief of Naval Research ATTN: Code ONR 439 N. Perrone Washington, DC 20360
1	Director US Army TRADOC Systems Analysis Activity ATTN: ATAA-SA White Sands Missile Range NM 88002	3	Commander US Naval Air Systems Command ATTN: AIR-604 Washington, DC 20360
		3	Commander US Naval Ordnance Systems Cmd ATTN: ORD-9132 Washington, DC 20360
		2	Commander US Naval Air Development Center, Johnsville Warminster, PA 18974
		1	Commander US Naval Missile Center Point Mugu, CA 93041

DISTRIBUTION LIST

<u>No. of Copies</u>	<u>Organization</u>	<u>No. of Copies</u>	<u>Organization</u>
2	Commander David W. Taylor Naval Ship Research & Development Ctr ATTN: Dr. Hans J. Lugt Bethesda, MD 20084	2	AFWL (WLL) Kirtland AFB, NM 87117
		1	AFFDL (FDT) Wright-Patterson AFB, OH 45433
2	Commander US Naval Surface Weapons Center Silver Spring, MD 20910	2	AFML Wright-Patterson AFB, OH 45433
4	Commander US Naval Surface Weapons Center ATTN: Code TEB D. W. Colbertson Mr. L. Hock Code TX, Dr. W. Soper Dahlgren, VA 22448	3	ASD (YH/EX, John Rievley; XRHD, Gerald Bennett; ENYS, Matt Kolléck) Wright-Patterson AFB, OH 45433
		1	Headquarters National Aeronautics and Space Administration Washington, DC 20546
3	Commander US Naval Weapons Center ATTN: Code 4057 Code 5114, Dr. Lundstrom Code 6031, Mr. Backman China Lake, CA 93555	1	Director Jet Propulsion Laboratory ATTN: Lib (TDS) 4800 Oak Grove Drive Pasadena, CA 91103
4	Commander US Naval Research Laboratory ATTN: Mr. W. J. Ferguson Mr. J. Baker Dr. H. Pusey Dr. F. Rosenthal Washington, DC 20375	4	Director National Aeronautics and Space Administration Langley Research Center Langley Station Hampton, VA 23365
1	Superintendent US Naval Postgraduate School ATTN: Dir of Lib Monterey, CA 93940	1	Director National Aeronautics and Space Administration Manned Spacecraft Center ATTN: Lib Houston, TX 77058
1	ADTC/DLJW, CPT D. Matuska Eglin AFB, FL 32542	2	Aerospace Corporation ATTN: Mr. R. Kennel Mr. L. G. King P. O. Box 95085 Los Angeles, CA 90045
1	AFATL/DL DL, MAJ J.E. Morgan and Mr. Leo Wilson) Eglin AFB, FL 32542		

DISTRIBUTION LIST

<u>No. of Copies</u>	<u>Organization</u>	<u>No. of Copies</u>	<u>Organization</u>
1	Boeing Aerospace Company ATTN: R.G. Blaisdell (M.S. 40-25) Seattle, WA 98124	3	Sandia Laboratories ATTN: Dr. W. Herrmann Dr. L. Bertholf Dr. J. W. Nunziato Albuquerque, NM 87115
1	Dupont Experimental Labs ATTN: Mr. J. Lupton Dr. C. Zweben Wilmington, DE 19801	2	Systems, Science and Software, Inc. ATTN: Dr. R. Sedgwick Ms. L. Hageman P. O. Box 1620 La Jolla, CA 92038
1	Falcon R&D ATTN: Mr. R. Miller 1225 S. Huron Street Denver, CO 80223	1	3C Systems, Inc. ATTN: Mr. M. Kornhauser 620 Argyle Road Wynnewood, PA 19096
2	Falcon R&D, Thor Facility ATTN: Mr. D. Malick Mr. J. Wilson 696 Fairmount Avenue Baltimore, MD 21204	3	Brown University Division of Engineering ATTN: Prof. P. Marcal Prof. H. Kolsky Prof. P. Symonds Providence, RI 02192
1	President General Research Corporation ATTN: Lib McLean, VA 22101	2	University of California Lawrence Livermore Laboratory ATTN: Mr. M. Wilkins Mr. M. Van Thiel P. O. Box 808 Livermore, CA 94550
3	Honeywell, Inc. Government & Aerospace Products Division ATTN: Mr. J. Blackburn Dr. G. Johnson Mr. R. Simpson 600 Second Street, NE Hopkins, NM 55343	4	University of California Los Alamos Scientific Lab ATTN: Dr. J. Walsh Dr. L. Hantel Dr. B. Craig Dr. J. Dienes Los Alamos, NM 87545
2	Physics International Company ATTN: Dr. D. Orphal Dr. C. Godfrey 2700 Merced San Leandro, CA 94577		<u>Aberdeen Proving Ground</u> Marine Corps Ln Ofc Dir, USAMSAA Cdr, USATECOM ATTN: Mr. W. Pless Mr. S. Keithley
1	Rockwell Corporation ATTN: Mr. W. Jackson 10301 Overhill Drive Santa Anna, CA 92705		